

SILVERRUSH. XI. Intensity Mapping for Ly α Emission Extending over 100-1000 comoving kpc around $z \sim 2 - 7$ LAEs with Subaru HSC-SSP and CHORUS Data

SHOTARO KIKUCHIHARA,^{1,2} YUICHI HARIKANE,^{1,3} MASAMI OUCHI,^{1,4,5,6} YOSHIKI ONO,¹ TAKATOSHI SHIBUYA,⁷
RYOHEI ITOH,^{1,8} RYOTA KAKUMA,^{1,2} AKIO K. INOUE,^{9,10} HARUKA KUSAKABE,¹¹ KAZUHIRO SHIMASAKU,^{2,12}
RIEKO MOMOSE,² YUMA SUGAHARA,^{4,9} SATOSHI KIKUTA,¹³ SHUN SAITO,¹⁴ NOBUNARI KASHIKAWA,^{2,12} HAIBIN ZHANG,¹⁵
AND CHIEN-HSIU LEE¹⁶

¹*Institute for Cosmic Ray Research, The University of Tokyo, 5-1-5 Kashiwanoha, Kashiwa, Chiba 277-8582, Japan*

²*Department of Astronomy, Graduate School of Science, The University of Tokyo, 7-3-1 Hongo, Bunkyo-ku, Tokyo 113-0033, Japan*

³*Department of Physics and Astronomy, University College London, Gower Street, London WC1E 6BT, UK*

⁴*National Astronomical Observatory of Japan, 2-21-1 Osawa, Mitaka, Tokyo 181-8588, Japan*

⁵*Graduate University for Advanced Studies (SOKENDAI), 2-21-1 Osawa, Mitaka, Tokyo 181-8588, Japan*

⁶*Kavli Institute for the Physics and Mathematics of the Universe (Kavli IPMU, WPI), The University of Tokyo, 5-1-5 Kashiwanoha, Kashiwa, Chiba 277-8583, Japan*

⁷*Kitami Institute of Technology, 165 Koen-cho, Kitami, Hokkaido 090-8507, Japan*

⁸*Department of Physics, Graduate School of Science, The University of Tokyo, 7-3-1 Hongo, Bunkyo-ku, Tokyo 113-0033, Japan*

⁹*Waseda Research Institute for Science and Engineering, Faculty of Science and Engineering, Waseda University, 3-4-1 Okubo, Shinjuku, Tokyo 169-8555, Japan*

¹⁰*Department of Physics, School of Advanced Science and Engineering, Faculty of Science and Engineering, Waseda University, 3-4-1 Okubo, Shinjuku, Tokyo 169-8555, Japan*

¹¹*Observatoire de Genève, Université de Genève, 51 chemin de Pégase, 1290 Versoix, Switzerland*

¹²*Research Center for the Early Universe, Graduate School of Science, The University of Tokyo, 7-3-1 Hongo, Bunkyo-ku, Tokyo 113-0033, Japan*

¹³*Center for Computational Sciences, University of Tsukuba, Ten-nodai, 1-1-1 Tsukuba, Ibaraki 305-8577, Japan*

¹⁴*Institute for Multi-messenger Astrophysics and Cosmology, Department of Physics, Missouri University of Science and Technology, 1315 N. Pine Street, Rolla, MO 65409, USA*

¹⁵*Department of Astronomy, Tsinghua University, No. 1 Qinghuayuan, Beijing 100084, China*

¹⁶*NSF's National Optical-Infrared Astronomy Research Laboratory, Tucson, AZ 85719, USA*

Submitted to ApJ

ABSTRACT

We conduct intensity mapping to probe for extended diffuse Ly α emission around Ly α emitters (LAEs) at $z \sim 2 - 7$, exploiting very deep (~ 26 mag at 5σ) and large-area (~ 4.5 deg²) Subaru/Hyper Suprime-Cam narrow-band (NB) images and large LAE catalogs consisting of a total of 1781 LAEs at $z = 2.2, 3.3, 5.7,$ and 6.6 obtained by the HSC-SSP SILVERRUSH and CHORUS projects. We calculate the spatial correlations of these LAEs with $\sim 1 - 2$ billion pixel flux values of the NB images, deriving the average Ly α surface brightness ($SB_{\text{Ly}\alpha}$) radial profiles around the LAEs. By carefully estimating systematics such as fluctuations of sky background and point spread functions, we detect diffuse Ly α emission ($\sim 10^{-20} - 10^{-19}$ erg s⁻¹ cm⁻² arcsec⁻²) at 100 – 1000 comoving kpc around $z = 3.3$ LAEs at the 4.1σ level and tentatively ($\sim 2\sigma$) at the other redshifts, beyond the virial radius of a dark-matter halo with a mass of $10^{11} M_{\odot}$. While the observed $SB_{\text{Ly}\alpha}$ profiles have similar amplitudes at $z = 2.2 - 6.6$ within the uncertainties, the intrinsic $SB_{\text{Ly}\alpha}$ profiles (corrected for the cosmological dimming effect) increase toward high redshifts. This trend may be explained by increasing hydrogen gas density due to the evolution of the cosmic volume. Comparisons with theoretical models suggest that extended Ly α emission around a LAE is powered by resonantly scattered Ly α photons in the CGM and IGM that originates from the inner part of the LAE, and/or neighboring galaxies around the LAE.

Keywords: galaxies: formation — galaxies: evolution — galaxies: high-redshift — galaxies: halos — intergalactic medium

1. INTRODUCTION

The gas surrounding a galaxy, called the circumgalactic medium (CGM), falls into the galaxy and triggers star formation activity, and is subsequently ejected from the galaxy due to outflows (e.g., Tumlinson et al. 2017; Péroux & Howk 2020). The hydrogen gas inside the CGM can be traced by Lyman-alpha ($\text{Ly}\alpha$) emission, which is observed as a $\text{Ly}\alpha$ halo (LAH). Therefore, observing LAHs is key to understanding the properties and kinematics of the CGM, and eventually provide information on galaxy formation and evolution.

Many studies have detected LAHs around nearby galaxies (e.g., Östlin et al. 2009; Hayes et al. 2013, 2014). At high-redshift ($z > 2$), meanwhile, LAHs have been identified mainly around massive galaxies, such as Lyman break galaxies (e.g., Hayashino et al. 2004; Swinbank et al. 2007; Steidel et al. 2011) and quasars (e.g., Goto et al. 2009; Cantalupo et al. 2014; Martin et al. 2014; Borisova et al. 2016; Arrigoni Battaia et al. 2019; Kikuta et al. 2019; Zhang et al. 2020). However, it remains difficult to detect diffuse emission around less massive star-forming galaxies (SFGs), such as $\text{Ly}\alpha$ emitters (LAEs), at high redshift, due to their faintness and sensitivity limits.

To overcome this difficulty, Rauch et al. (2008), for example, performed a very deep (92 hr) long-slit observation with the ESO Very Large Telescope (VLT)/FOcal Reducer and low dispersion Spectrograph 2 (FOR2) that reached a 1σ surface brightness (SB) detection limit of $8 \times 10^{-20} \text{ erg cm}^{-2} \text{ s}^{-1} \text{ arcsec}^{-2}$. They investigated 27 LAEs at $z = 2.67 - 3.75$, identifying $\text{Ly}\alpha$ emission extending over 26 physical kpc (pkpc) around one of the LAEs. Individual detections of many high redshift LAHs have been enabled by the advent of the Multi-Unit Spectroscopic Explorer (MUSE) installed on the VLT. Recently, Leclercq et al. (2017) identified individual LAHs around 145 LAEs at $z = 3 - 6$ in the Hubble Ultra Deep Field (HUDF) with the VLT/MUSE (see also Wisotzki et al. 2016). Their data reached a SB limit of $\lesssim 10^{-19} \text{ erg s}^{-1} \text{ cm}^{-2} \text{ arcsec}^{-2}$ at radii of > 10 pkpc. The magnification effect caused by gravitational lensing was also utilized in conjunction with the MUSE for studying individual LAHs (Patrício et al. 2016; Smit et al. 2017; Claeysens et al. 2019).

A stacking method has been widely used to obtain averaged LAH profiles with high signal-to-noise (S/N) ratios (e.g., Matsuda et al. 2012; Momose et al. 2014, 2016; Xue et al. 2017; Wisotzki et al. 2018; Wu et al.

2020). For example, Momose et al. (2014) stacked > 100 narrow-band (NB) images around LAEs at $z = 2.2 - 6.6$ using Subaru Telescope/Suprime-Cam (SC) data, investigating LAH profiles up to ~ 50 pkpc radial scales. Matsuda et al. (2012) and Momose et al. (2016) investigated the LAH size dependence on LAE properties, such as $\text{Ly}\alpha$ luminosity, rest-frame ultra-violet (UV) magnitude, and overdensity, at $z = 3.1$ and 2.2 , respectively. We note that some studies (e.g. Bond et al. 2010; Feldmeier et al. 2013; Jiang et al. 2013) reported no evidence of extended $\text{Ly}\alpha$ emission at $z > 2$.

Another approach is the intensity mapping technique (Kovetz et al. 2017 for a review; see also Carilli 2011; Gong et al. 2011; Silva et al. 2013; Pullen et al. 2014; Comaschi & Ferrara 2016a,b; Li et al. 2016; Fonseca et al. 2017), which utilizes cross-correlation functions between objects and their emission or absorption spectra. This technique enables us to detect signals from targeted galaxies with a high S/N ratio by efficiently estimating and removing contaminating signals from foreground interlopers. Croft et al. (2016, 2018) derived cross-correlation functions between the $\text{Ly}\alpha$ emission and quasar positions at $z = 2 - 3.5$ using data from the Sloan Digital Sky Survey (SDSS; Eisenstein et al. 2011) Baryon Oscillation Spectroscopic Survey (BOSS; Dawson et al. 2013). This work enabled the detection of positive signals up to a $\sim 15 h^{-1}$ comoving Mpc (cMpc) radial scale.

Recently, Kakuma et al. (2021) applied the intensity mapping technique to LAEs at $z = 5.7$ and 6.6 using Subaru/Hyper Suprime-Cam (HSC) data. They tentatively identified very diffuse ($\sim 10^{-20} \text{ erg s}^{-1} \text{ cm}^{-2} \text{ arcsec}^{-2}$) $\text{Ly}\alpha$ emission extended around the LAEs over the radial scale of the virial radius (R_{vir}) of a dark-matter halo (DMH). Although their finding has shed light on the potential existence of $\text{Ly}\alpha$ -emitting hydrogen gas beyond R_{vir} around LAEs in the reionization epoch, it remains an open question whether LAEs host such extended structures even at lower redshifts ($z < 5$). In this paper, we exploit NB images offered in two Subaru/HSC surveys, the Cosmic Hydrogen Reionization Unveiled with Subaru (CHORUS; Inoue et al. 2020) and the Subaru Strategic Program (HSC-SSP; Aihara et al. 2019), which enable us to trace $\text{Ly}\alpha$ emission from LAEs across $z = 2.2 - 6.6$. Our goal is to systematically investigate diffuse $\text{Ly}\alpha$ emission extended beyond R_{vir} around $z = 2.2 - 6.6$ LAEs, taking

advantage of the intensity mapping technique and ultra-deep images from the CHORUS and HSC-SSP projects.

Another open question about extended $\text{Ly}\alpha$ emission is its physical origin (see review by Ouchi et al. 2020 and Figure 15 of Momose et al. 2016). Theoretical studies have suggested several physical processes producing a LAH around a galaxy, which can be attributed mainly to 1) resonant scattering and 2) *in-situ* production. 1) Resonant scattering: $\text{Ly}\alpha$ photons are produced in the interstellar medium (ISM) of the galaxy, and then resonantly scattered by neutral hydrogen gas while escaping the galaxy into the CGM and intergalactic medium (IGM) (e.g., Laursen & Sommer-Larsen 2007; Laursen et al. 2011; Steidel et al. 2011; Zheng et al. 2011; Dijkstra & Kramer 2012; Jeon-Daniel et al. 2012; Verhamme et al. 2012; Kakiichi & Dijkstra 2018; Smith et al. 2018, 2019; Garel et al. 2021). 2) *In-situ* production: $\text{Ly}\alpha$ photons are produced not inside the galaxy but in the CGM. This can be further classified into three processes: i) recombination, ii) collisional excitation, and iii) satellite galaxies. i) Recombination: ionizing radiation from the galaxy or extragalactic background (UVB) photoionizes the hydrogen gas in the CGM, which in turn emit $\text{Ly}\alpha$ emission via recombination (‘fluorescence’; e.g., Furlanetto et al. 2005; Cantalupo et al. 2005; Kollmeier et al. 2010; Lake et al. 2015; Mas-Ribas & Dijkstra 2016; Gallego et al. 2018; Mas-Ribas et al. 2017b). ii) Collisional excitation: Hydrogen gas in the CGM is compressively heated by shocks and then emit $\text{Ly}\alpha$ photons by converting its gravitational energy into $\text{Ly}\alpha$ emission when they accrete onto the galaxy (‘gravitational cooling’ or ‘cold stream’; e.g., Haiman et al. 2000; Fardal et al. 2001; Goerdt et al. 2010; Faucher-Giguère et al. 2010; Rosdahl & Blaizot 2012; Lake et al. 2015). iii) Satellite galaxies: $\text{Ly}\alpha$ emission is produced by star formation (SF) in unresolved dwarfs surrounding the galaxy (‘satellite galaxies’; e.g., Mas-Ribas et al. 2017a,b). To recognize which process plays a major role, Kakuma et al. (2021) compared the observed $\text{Ly}\alpha$ SB profiles against the prediction by Zheng et al. (2011) that considers resonant scattering, although large uncertainties of the data prevented to draw a conclusion. Since their comparison was limited to the case for resonant scattering at $z = 5.7$, we need to systematically investigate various origins by utilizing multiple models at multiple redshifts to pin down the key origin(s), in the similar way as Byrohl et al. (2020) and Mitchell et al. (2021).

This paper is organized as follows. Our data are described in Section 2. In Section 3, we use the intensity mapping technique to derive the cross-correlation SB of $\text{Ly}\alpha$ emission around the LAEs. We discuss the redshift

evolution and physical origins of extended $\text{Ly}\alpha$ emission in Section 4 and summarize our findings in Section 5.

Throughout this paper, magnitudes are given in the AB system (Oke & Gunn 1983). We adopt the concordance cosmology with $\Omega_{\text{m},0} = 0.7$, $\Omega_{\Lambda,0} = 0.3$, and $H_0 = 70 \text{ km s}^{-1} \text{ Mpc}^{-1}$, where $1''$ corresponds to transverse sizes of (8.3, 7.5, 5.9, 5.4) pkpc and (26, 32, 39, 41) comoving kpc (ckpc) at $z = (2.2, 3.3, 5.7, 6.6)$.

2. DATA

In this Section, we describe the images and sample catalogs used for our analyses. All the images and catalogs are based on Subaru/HSC data.

2.1. Images

We use NB and broad-band (BB) imaging data that were obtained in two Subaru/HSC surveys, the HSC-SSP and the CHORUS. The HSC-SSP and CHORUS data were obtained in March 2014-January 2018 and January 2017-December 2018, respectively. We specifically use the internal data of the S18A release. The HSC-SSP survey is a combination of three layers: Wide, Deep, and UltraDeep (UD). We use the UD layer images in the fields of the Cosmological Evolution Survey (UD-COSMOS; Scoville et al. 2007) and Subaru/XMM Deep Survey (UD-SXDS; Sekiguchi et al. 2005), because the wide survey areas ($\sim 2 \text{ deg}^2$ for each field) and deep imaging (the 5σ limiting magnitudes are ~ 26 mag in a $2''$ -diameter aperture) in these fields are advantageous for the detection of very diffuse $\text{Ly}\alpha$ emission. The CHORUS data were obtained over the UD-COSMOS field. The HSC-SSP and CHORUS data were reduced with the HSC pipeline v6.7 (Bosch et al. 2018).

The HSC-SSP program of S18A provides the data of two NB (NB816 and NB921) filters in the UD-COSMOS and UD-SXDS fields, while the CHORUS images are offered in four NB (NB387, NB527, NB718, and NB973) filters in the UD-COSMOS field. In this work, we present the results in the NB387, NB527, NB816, and NB921 filters. The NB718 and NB973 filters are not used in the following sections, because the number of LAEs and the image depths are not sufficient to detect diffuse $\text{Ly}\alpha$ emission. The NB387, NB527, NB816, and NB921 filters are centered at 3863, 5260, 8177, and 9215 Å with the full widths at half maximum (FWHMs) of 55, 79, 113, and 135 Å, respectively, which cover the observed wavelengths of $\text{Ly}\alpha$ emission from $z = 2.178 \pm 0.023$, 3.327 ± 0.032 , 5.726 ± 0.046 , and 6.580 ± 0.056 , respectively. Five BB (g -, $r2$ -, $i2$ -, z -, and y -band) filters are also available in both HSC-SSP and CHORUS. Figure 1 shows the NB and BB filter throughputs, and Table 1 summarizes the images and filters.

Table 1. Summary of the NB filters and images.

NB	λ_c (Å)	FWHM (Å)	z_{LAE}	UD-COSMOS		UD-SXDS	
				Area (deg ²)	$m_{\text{NB},5\sigma}$ (mag)	Area (deg ²)	$m_{\text{NB},5\sigma}$ (mag)
(1)	(2)	(3)	(4)	(5)	(6)	(7)	(8)
NB387 (CHORUS)	3863	55	2.178 ± 0.023	1.561	25.67	—	—
NB527 (CHORUS)	5260	79	3.327 ± 0.032	1.613	26.39	—	—
NB816 (HSC-SSP)	8177	113	5.726 ± 0.046	2.261	25.75	2.278	25.61
NB921 (HSC-SSP)	9215	135	6.580 ± 0.056	2.278	25.48	2.278	25.31

NOTE—Columns: (1) NB filter. (2)-(3) Central wavelength (λ_c) and FWHM of the NB filter transmission curve. (4) Redshift range of the LAEs whose Ly α emission enters the NB filter. (5)-(6) Effective area and 5σ limiting NB magnitude ($m_{\text{NB},5\sigma}$) in the UD-COSMOS field. The $m_{\text{NB},5\sigma}$ value is measured with a $2''$ -diameter aperture in each patch, and then averaged over the field. See Inoue et al. (2020) and Hayashi et al. (2020) for the spatial variance of $m_{\text{NB},5\sigma}$. The $m_{\text{NB},5\sigma}$ value in NB387 is corrected for the systematic zero-point offset by 0.45 mag (see Section 2.2). (7)-(8) Same as Columns (5)-(6), but for the UD-SXDS field. The values in this Table are cited from Ono et al. (2021).

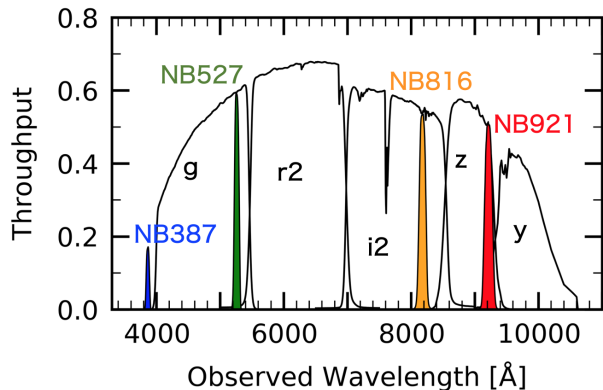


Figure 1. Effective response curves of the HSC NB filters: NB387 (blue), NB527 (green), NB816 (orange), and NB921 (red), and BB filters: *g*, *r2*, *i2*, *z*, and *y* (black). These response curves include the quantum efficiency of the HSC CCD, transmittance of the dewar window and of the Primary Focus Unit, reflectivity of the Primary Mirror, and airmass at the Telescope site.

Bright sources in the NB and BB images must be masked since they contaminate diffuse emission. We thus mask pixels flagged with either `DETECT` or `BRIGHT_OBJECT` using the masks provided by the HSC pipeline (termed *original* masks). A pixel is flagged with `DETECT` or `BRIGHT_OBJECT` when the pixel is covered by a detected ($\geq 5\sigma$) object or is affected by nearby bright sources, respectively. However, because a part of bright sources were missed in the *original* masks due to bad photometry, the HSC-SSP team offered new masks that mitigated this problem (hereafter termed *revised*

masks).¹ We adopt the *revised* masks in addition to the *original* masks to flag `BRIGHT_OBJECT`. We use the *revised* *g*-, *r2*-, *z*-, and *y*-band masks for NB387, NB527, NB816, and NB921 images, respectively, because the *revised* masks are offered only in the BB filters. For the BB images, we use the *revised* masks defined for each BB filter. We visually confirm that these criteria successfully cover bright sources and contaminants in the images.

2.2. LAE Samples

We use the LAE catalog constructed by Ono et al. (2021) as a part of the Systematic Identification of LAEs for Visible Exploration and Reionization Research Using Subaru HSC (SILVERRUSH) project (Ouchi et al. 2018, see also Shibuya et al. 2018a,b; Konno et al. 2018; Harikane et al. 2018; Inoue et al. 2018; Higuchi et al. 2019; Harikane et al. 2019; Kakuma et al. 2021). Ono et al. (2021) selected LAE candidates based on color and removed contaminants by a convolutional neural network (CNN) and visual inspection. Their final catalog includes (542, 959, 395, 150) LAEs at $z = (2.2, 3.3, 5.7, 6.6)$ in the UD-COSMOS field, and (560, 75) LAEs at $z = (5.7, 6.6)$ in the UD-SXDS field.

The NB images of the UD-COSMOS and UD-SXDS fields are deepest at the center and become shallower toward the edges (Hayashi et al. 2020; Inoue et al. 2020). We thus exclude LAEs outside of the boundaries that are shown with the black dashed circles in Figures 2 and 3.

¹ <https://hsc-release.mtk.nao.ac.jp/doc/index.php/bright-star-masks-2/>

We estimate the $\text{Ly}\alpha$ line luminosities ($L_{\text{Ly}\alpha}$) following Shibuya et al. (2018a, see also Itoh et al. 2018). First, we measure the NB (BB) magnitudes m_{NB} (m_{BB}) of the LAEs at $z = 2.2, 3.3, 5.7,$ and 6.6 in the NB387 (g -band), NB527 ($r2$ -band), NB816 (z -band), and NB921 (y -band) filters, respectively. The magnitudes are measured with a $2''$ -diameter aperture because it efficiently covers the point spread function (PSF), whose FWHM is $0''.8 - 1''.1$ (Ono et al. 2021). The NB387 magnitudes are corrected for the systematic zero-point offset by 0.45 mag, following the recommendation by the HSC-SSP team.² Next, we follow Shibuya et al. (2018a) in our derivation of the $\text{Ly}\alpha$ line fluxes ($f_{\text{Ly}\alpha}$) from m_{NB} and m_{BB} , assuming a flat UV continuum and the IGM attenuation model taken from Inoue et al. (2014). Lastly, the values of $L_{\text{Ly}\alpha}$ are derived via $L_{\text{Ly}\alpha} = 4\pi d_{\text{L}}(z_{\text{LAE}})^2 f_{\text{Ly}\alpha}$, where $d_{\text{L}}(z_{\text{LAE}})$ denotes the luminosity distance to the LAE at redshift z_{LAE} .

Although the completeness of the LAEs is as high as $\gtrsim 90\%$ at $m_{\text{NB}} \lesssim 24.5$ in the CNN of Ono et al. (2021), faint LAEs may be missed in the observations and selection. To ensure completeness, we use only LAEs whose $L_{\text{Ly}\alpha}$ values are larger than the modes (peaks) of the $L_{\text{Ly}\alpha}$ histograms, which are represented as $L_{\text{Ly}\alpha}^{\text{min}}$ in Table 2. This sample, termed the *all* sample, consists of (289, 762, 210, 56) LAEs at $z = (2.2, 3.3, 5.7, 6.6)$ and (393, 24) LAEs at $z = (5.7, 6.6)$ in the UD-COSMOS and UD-SXDS fields, respectively. To accurately compare the LAEs of different redshifts at similar $L_{\text{Ly}\alpha}$ values, we further exclude faint LAEs from the *all* sample such that the mean $L_{\text{Ly}\alpha}$ values are equal to $10^{42.9} \text{ erg s}^{-1}$ at each redshift. This selection results in (37, 123, 125) LAEs at $z = (2.2, 3.3, 5.7)$ and 313 LAEs at $z = 5.7$ in the UD-COSMOS and UD-SXDS fields, respectively, which we hereafter refer to as the *bright* subsample. At $z = 6.6$, since the mean $L_{\text{Ly}\alpha}$ values of the *all* sample are $10^{43.0} \text{ erg s}^{-1}$ in both the UD-COSMOS and UD-SXDS fields, we also use the *all* sample as the *bright* subsample. In summary, we use a total of 1781 and 717 LAEs in the UD-COSMOS+UD-SXDS fields as the *all* sample and the *bright* subsample, respectively. The $L_{\text{Ly}\alpha}$ values and sample sizes are summarized in Table 2. The sky distributions of the LAEs in the UD-COSMOS and UD-SXDS fields are presented in Figures 2 and 3, respectively.

A major update of our data compared to Kakuma et al. (2021) is that we add new 1051 LAEs at $z = 2.2$ and 3.3 using the CHORUS data. The catalog of $z = 5.7$

and 6.6 LAEs are also updated in that we use the latest catalog constructed by Ono et al. (2021) based on HSC-SSP S18A images, while Kakuma et al. (2021) used the S16A catalog taken from Shibuya et al. (2018a). Although the number of the LAEs increased owing to the improved limiting magnitudes, we excluded faint LAEs from those included in Ono et al. (2021), which resulting in comparable numbers of the LAEs between Kakuma et al. (2021)’s and our *all* samples. The sky and $L_{\text{Ly}\alpha}$ distributions are also similar between these two samples. We use the same images as Kakuma et al. (2021, i.e., those taken from the HSC-SSP S18A release) in NB816 and NB921, while our masking prescription may be slightly different.

2.3. NonLAE Samples

Although the intensity mapping technique can remove spurious signals from low-redshift interlopers, other systematics, such as the sky background and PSF, may still contaminate LAE signals. To estimate the contribution from these systematics, we use foreground sources, which we hereafter term “NonLAEs.” Because NonLAEs should correlate only with the systematics, but not with $\text{Ly}\alpha$ emission from LAEs, we estimate these systematics by applying the intensity mapping technique to NonLAEs.

We construct NonLAE samples as follows. First, we detect sources in the NB images using SExtractor (Bertin & Arnouts 1996). Second, we select only sources that are sufficiently bright ($\lesssim 26$ mag) in the g -, $r2$ -, and $i2$ -bands, to remove spurious sources and artifacts. Third, we randomly select the sources such that they have the same sky, FWHM, and m_{NB} distributions as those of the LAEs in each field at each redshift. In this way, $\sim 10^3$ sources are selected, which we define as NonLAEs (see Figure 4 for the FWHM- m_{NB} distributions of the $z = 3.3$ LAEs and corresponding NonLAEs). We note that only $< 1\%$ of the NonLAEs meet the color selection criteria of LAEs defined by Ono et al. (2021, see their Section 2).

3. INTENSITY MAPPING ANALYSIS

In this section, we derive the SB radial profiles of $\text{Ly}\alpha$ emission around the LAEs using the intensity mapping technique.

3.1. Cross-correlation Functions

We compute SB as a cross-correlation function between given band (XB) emission intensities and given

² <https://hsc-release.mtk.nao.ac.jp/doc/index.php/known-problems-2/#hsc-link-10>

Table 2. Summary of the sample.

z_{LAE}	<i>all</i> sample						<i>bright</i> subsample					
	UD-COSMOS			UD-SXDS			UD-COSMOS			UD-SXDS		
	$L_{\text{Ly}\alpha}^{\text{min}}$	$L_{\text{Ly}\alpha}^{\text{mean}}$	N_{LAE}	$L_{\text{Ly}\alpha}^{\text{min}}$	$L_{\text{Ly}\alpha}^{\text{mean}}$	N_{LAE}	$L_{\text{Ly}\alpha}^{\text{min}}$	$L_{\text{Ly}\alpha}^{\text{mean}}$	N_{LAE}	$L_{\text{Ly}\alpha}^{\text{min}}$	$L_{\text{Ly}\alpha}^{\text{mean}}$	N_{LAE}
(1)	(2)	(3)	(4)	(5)	(6)	(7)	(8)	(9)	(10)	(11)	(12)	(13)
2.2	42.2	42.5	289	—	—	—	42.6	42.9	37	—	—	—
3.3	42.1	42.5	762	—	—	—	42.6	42.9	123	—	—	—
5.7	42.6	42.8	210	42.5	42.8	393	42.7	42.9	125	42.6	42.9	313
6.6	42.8	43.0	56	42.9	43.0	24	42.8*	43.0*	56*	42.9*	43.0*	24*
Total			1317			464			341			376

NOTE—Columns: (1) Redshift. (2)-(3) Minimum and mean Ly α luminosity of the *all* sample LAEs in the UD-COSMOS field, measured with a 2''-diameter aperture and shown in units of log erg s $^{-1}$. (4) Number of the LAEs. The total number of the LAEs over $z = 2.2 - 6.6$ are shown in the bottom row. (5)-(7) Same as Columns (2)-(4), but for the *all* subsample in the UD-SXDS field. (8)-(13) Same as Columns (2)-(7), but for the *bright* subsample.

* At $z = 6.6$, we treat the *all* sample also as the *bright* subsample in each field (see Section 2.2).

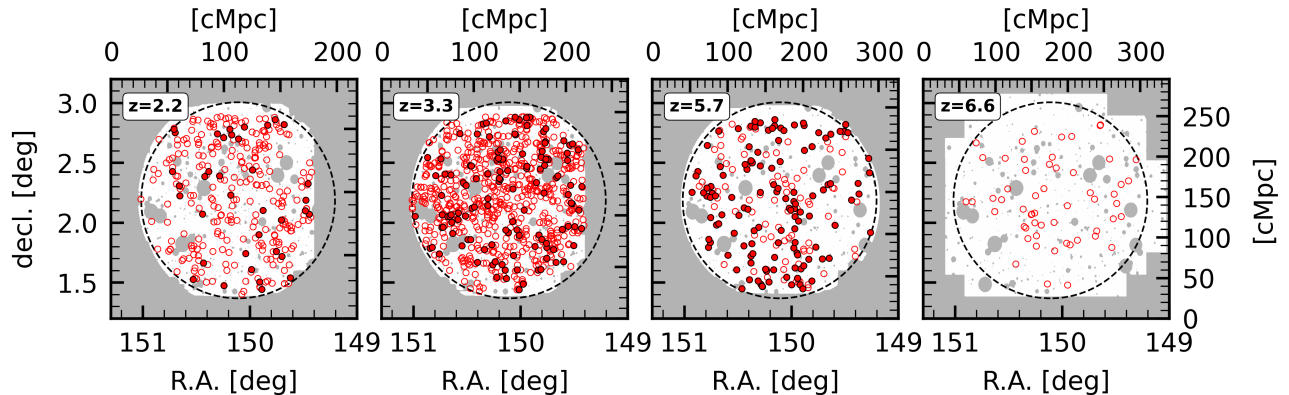


Figure 2. Sky distributions of the LAEs in the UD-COSMOS field at $z = 2.2, 3.3, 5.7,$ and 6.6 , from left to right. The open red circles show the positions of the LAEs included in the *all* sample but not in the *bright* subsample, while the filled red circles indicate those of the *bright* subsample LAEs (i.e., *all* sample LAEs are represented by the open+filled red circles). We use the LAEs inside the black dashed circles. The background white shades show the NB387, NB527, NB816, and NB921 images, from left to right. The gray shades show the regions where the pixel is masked or an UD image is not offered. Note that the distribution of the *bright* subsample at $z = 6.6$ is not displayed, because we treat the *all* sample also as the *bright* subsample at $z = 6.6$.

objects (OBJs), $\text{SB}_{\text{XB}\times\text{OBJ}}^3$, via

$$\text{SB}_{\text{XB}\times\text{OBJ},\nu}(r) = \frac{1}{N_{r,\text{OBJ}}} \sum_{i=1}^{N_{r,\text{OBJ}}} \mu_{\nu,i}^{(\text{XB})} \quad (1)$$

³ The right-hand side of Equation 1 represents a cross-correlation function, which has usually been referred to as ξ in previous work (e.g. Croft et al. 2016, 2018; Bielby et al. 2017; Momose et al. 2021b,a). However, we refer to this function as ‘SB,’ since the cross-correlation function is equivalent to surface brightness in our analyses.

and

$$\text{SB}_{\text{XB}\times\text{OBJ}}(r) = \text{SB}_{\text{XB}\times\text{OBJ},\nu}(r) \times \text{FWHM}_{\text{XB}}. \quad (2)$$

The pixel of the i -th pixel-OBJ pair has a pixel value of $\mu_{\nu,i}^{(\text{XB})}$ in the XB image in units of erg s $^{-1}$ cm $^{-2}$ Hz $^{-1}$ arcsec $^{-2}$. In NB387, we multiply $\mu_{\nu,i}^{(\text{NB387})}$ by 1.5 to correct for the zero-point offset of 0.45 mag (see Section 2.2). The summation runs over the $N_{r,\text{OBJ}}$ pixel-OBJ pairs that are separated by a spatial distance r . We use pixels at distances of between 1''.5 and 40'' from each OBJ (corresponding to the outer part of the CGM and

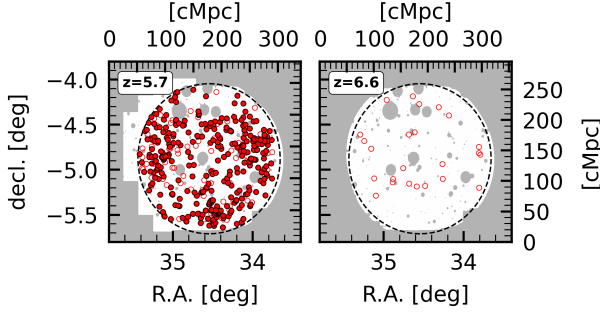


Figure 3. Same as Figure 2, but for the UD-SXDS field at $z = 5.7$ (left) and 6.6 (right).

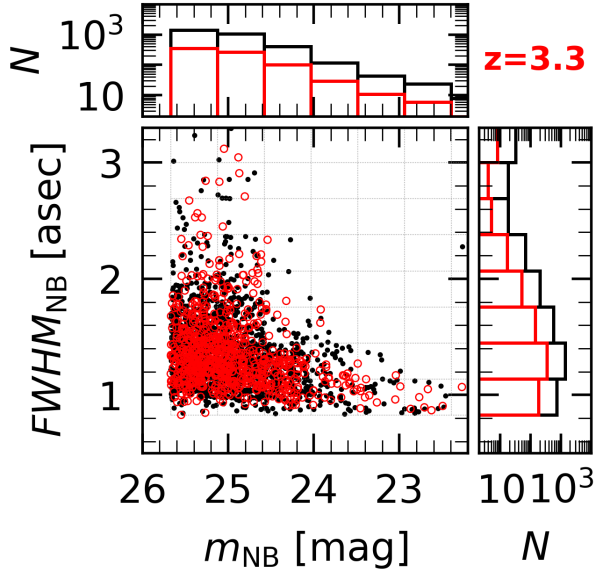


Figure 4. **Center:** NB FWHM (FWHM_{NB}) and magnitude (m_{NB}) distributions of the *all* sample at $z = 3.3$ (red circles), and the corresponding NonLAEs (black dots). **Top:** m_{NB} histogram of the LAEs and NonLAEs (red and black bars, respectively). **Right:** Same as the top panel, but for FWHM_{NB} .

outside), which were then divided into six radial bins. A total of $\sim (1 - 2) \times 10^9$ pixels were used for the calculation at each redshift. FWHM_{XB} represents the XB filter width (in units of Hz) corrected for IGM attenuation, derived via

$$\text{FWHM}_{\text{XB}} = \frac{\int_0^\infty e^{-\tau_{\text{eff}}(\nu)} T_{\text{XB}}(\nu) d\nu / \nu}{T_{\text{XB}}(\nu_\alpha) / \nu_\alpha}, \quad (3)$$

where $T_{\text{XB}}(\nu)$ denotes the transmittance of the XB filter, and ν_α is the the observed $\text{Ly}\alpha$ line frequency. We adopt the IGM optical depth $\tau_{\text{eff}}(\nu)$ from Inoue et al. (2014).

The statistical uncertainty of $\text{SB}_{\text{XB} \times \text{OBJ}}$ is estimated by the bootstrap method. We randomly resample objects while keeping the sample size and calculated $\text{SB}_{\text{XB} \times \text{OBJ}}$. We then repeat the resampling 10^4 times,

adopting the 1σ standard deviation of the $\text{SB}_{\text{XB} \times \text{OBJ}}$ values as the 1σ statistical uncertainty of the original $\text{SB}_{\text{XB} \times \text{OBJ}}$.

3.2. $\text{Ly}\alpha$ Surface Brightness

We estimate the SB of $\text{Ly}\alpha$ emission ($\text{SB}_{\text{Ly}\alpha}$) around the LAEs as follows. First, we subtract the systematics ($\text{SB}_{\text{NB} \times \text{NonLAE}}$) from the emission from the LAEs ($\text{SB}_{\text{NB} \times \text{LAE}}$) via

$$\text{SB}_{\text{NB}} = \text{SB}_{\text{NB} \times \text{LAE}} - \text{SB}_{\text{NB} \times \text{NonLAE}}. \quad (4)$$

Uncertainties in SB_{NB} propagate from those of $\text{SB}_{\text{NB} \times \text{LAE}}$ and $\text{SB}_{\text{NB} \times \text{NonLAE}}$. We present the radial profiles of the $\text{SB}_{\text{NB} \times \text{LAE}}$, $\text{SB}_{\text{NB} \times \text{NonLAE}}$, and SB_{NB} of the *all* sample and *bright* subsample in Figures 5 and 6, respectively.

We use Fisher's method (Fisher 1970) to estimate the S/N ratios of SB_{NB} over all the radial bins, following Kakuma et al. (2021). Generally, a p -value is expressed as

$$p = \int_{\text{S/N}}^\infty \mathcal{N}(x; \mu = 0, \sigma = 1) dx, \quad (5)$$

where $\mathcal{N}(x; \mu = 0, \sigma = 1)$ is a Gaussian distribution with an expected value $\mu = 0$ and a variance $\sigma^2 = 1$. We thus use this equation to convert the S/N ratio in the i -th radial bin (S/N_i) into the p -value in that bin (p_i). The χ^2 value over all the radial bins ($1 \leq i \leq N$), $\hat{\chi}^2$, is then calculated as $\hat{\chi}^2 = -2 \sum_{i=1}^N \ln(p_i)$. Since $\hat{\chi}^2$ follows a χ^2_{2N} distribution with $2N$ degrees of freedom, $\chi^2(x; \text{dof} = 2N)$, the p -value over all the radial bins, \hat{p} , is derived as

$$\hat{p} = \int_{\hat{\chi}^2}^\infty \chi^2(x; \text{dof} = 2N) dx. \quad (6)$$

We convert this to the S/N ratio over all the radial bins by solving Equation (5) for S/N. We use the radial bins at < 1 cMpc.

The black vertical dashed lines in Figures 5 and 6 indicate R_{vir} . Following the observational results by Ouchi et al. (2010) and Kusakabe et al. (2018), we assume that the DMHs hosting LAEs have halo masses (M_{halo}) of $10^{11} M_\odot$ at all the redshifts, which corresponds to a R_{vir} value of ~ 150 kpc.

As presented in Figures 5 and 6, at $z = 2.2$, we see no clear detection for the *all* sample, although $\text{SB}_{\text{NB} \times \text{LAE}}$ slightly exceeds $\text{SB}_{\text{NB} \times \text{NonLAE}}$ for the *bright* subsample with $\text{S/N} = 1.5$. At $z = 3.3$, SB_{NB} of the *all* sample is significantly positive over wide scales from ~ 100 ckpc to 1 cMpc with $\text{S/N} = 4.1$. At $z = 5.7$, SB_{NB} is significantly positive at $\sim 80 - 10^3$ ckpc for the *all* sample and *bright* subsample in the UD-COSMOS field

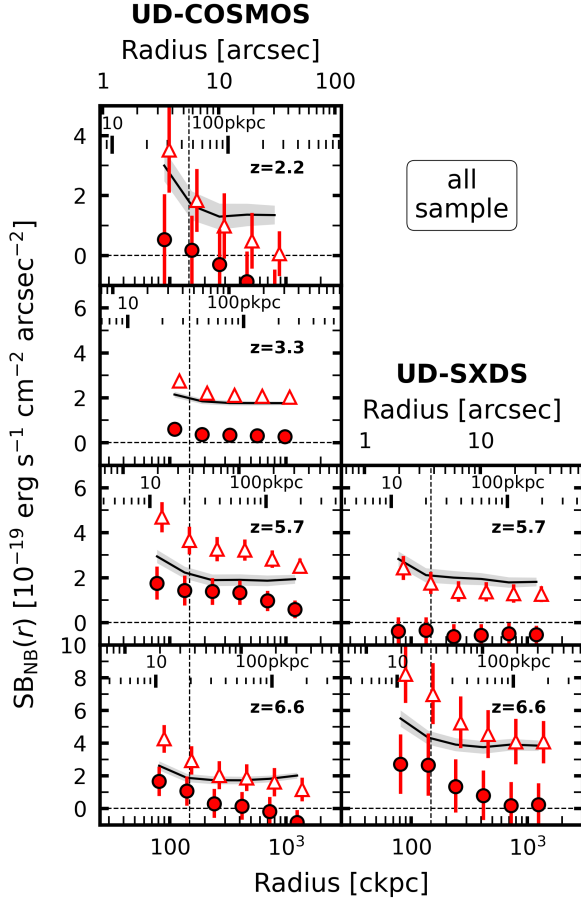


Figure 5. SB radial profiles of the *all* sample. **Left:** SB_{NB} in the UD-COSMOS field at $z = 2.2, 3.3, 5.7,$ and $6.6,$ from top to bottom. The red triangles and circles show SB before and after systematics subtraction ($SB_{NB \times LAE}$ and SB_{NB}), respectively. The black solid lines represent the systematics that are estimated with the NonLAEs ($SB_{NB \times NonLAE}$). The red error bars and gray shades are the 1σ uncertainties estimated by the bootstrap method. The vertical black dashed line represents R_{vir} of a DMH with $M_{halo} = 10^{11} M_{\odot}$, while the horizontal black line represents $SB = 0$. The upper, middle, and lower horizontal axes in each panel show radii in units of arcsec, pkpc, and ckpc, respectively. The data points of $SB_{NB \times LAE}$ are slightly shifted along the horizontal axis for clarity. **Right:** Same as the left column, but in the UD-SXDS field at $z = 5.7$ and 6.6 in the top and bottom panels, respectively. The S/N ratios of SB_{NB} are 4.1, 1.6, and 2.2 at $z = 3.3, 5.7,$ and $6.6,$ respectively (they are based on SB_{NB} averaged over the UD-COSMOS and UD-SXDS fields, at $z = 5.7$ and 6.6). There is no clear detection at $z = 2.2$.

with $S/N = 4.6$ and $4.1,$ respectively. Averaging SB_{NB} of the *all* sample in both fields with weights of the number of the LAEs in each field, we identify a tentatively positive signal with $S/N = 1.6$. At $z = 6.6,$ SB_{NB} are positive at $\sim 80 - 200$ ckpc in both fields. Averaging SB_{NB} over the two fields, we tentatively identify a positive signal with $S/N = 2.3$. We find that the emission

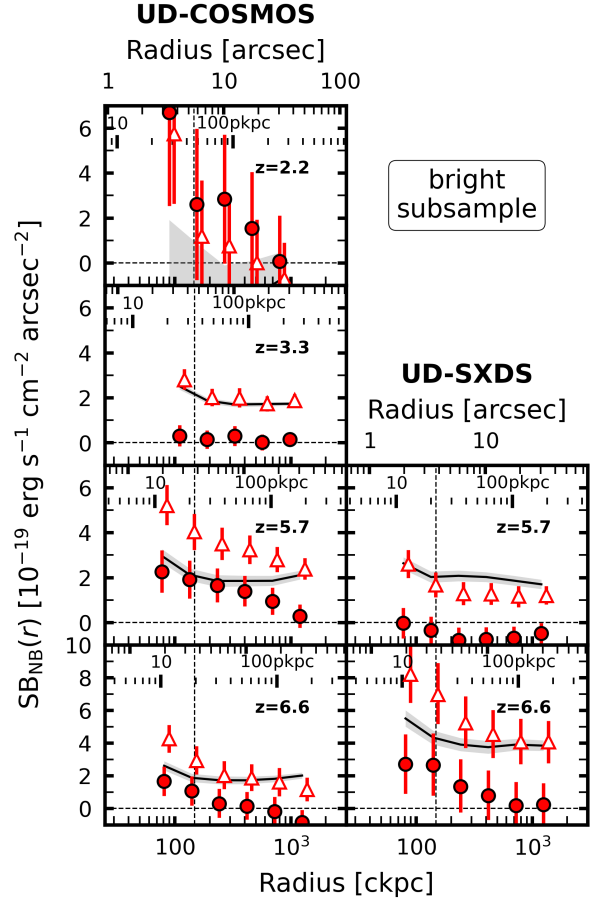


Figure 6. Same as Figure 5, but for the *bright* subsample. The S/N ratios of SB_{NB} are 1.5 and 1.4 at $z = 2.2$ and $5.7,$ respectively, while there is no clear detection at $z = 3.3$. The results at $z = 6.6$ (bottom panels) are the same as those in Figure 5 since we treat the *all* sample also as the *bright* subsample at $z = 6.6$.

SB at $z = 3.3 - 6.6$ is as diffuse as $\sim 10^{-20} - 10^{-19}$ erg $s^{-1} cm^{-2} arcsec^{-2}$. We note that $SB_{NB \times LAE}$ in the UD-SXDS field are systematically lower than $SB_{NB \times NonLAE},$ as reported in Kakuma et al. (2021).

UV continuum emission might contribute to the SB_{NB} in addition to the $Ly\alpha$ line emission. We thus estimate SB of the UV continuum emission, $SB_{cont,\nu},$ using

$$SB_{cont,\nu} < SB_{BB,\nu} \equiv SB_{BB \times LAE,\nu} - SB_{BB \times random,\nu}, \quad (7)$$

where $SB_{BB \times LAE,\nu}$ ($SB_{BB \times random,\nu}$) represents the SB value that is derived from the cross-correlation function between the BB images and LAEs (random sources) in units of erg $s^{-1} cm^{-2} Hz^{-1} arcsec^{-2}$. To estimate the sky background, we use random sources, not NonLAEs, since it is difficult to match the $FWHM_{NB} - m_{NB}$ distributions of NonLAEs with those of the LAEs due to faintness of the LAEs in the BB. Since $SB_{BB \times random,\nu}$ neglects signals from the PSF, $SB_{BB,\nu}$ should

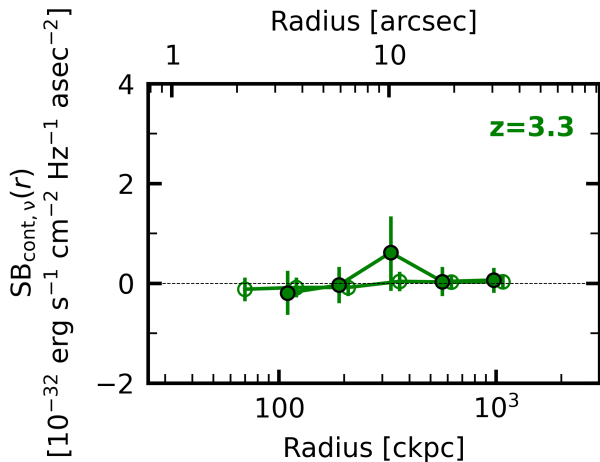


Figure 7. Radial profiles of the UV continuum SB of the *all* sample (open) and *bright* subsample (filled) at $z = 3.3$. The profiles are averages weighted with the number of the LAEs in the UD-COSMOS and UD-SXDS fields. The data points for *bright* subsample are slightly shifted along the horizontal axis for clarity. The data points should be treated as upper limits, since $\text{SB}_{\text{cont},\nu}$ neglects signals from the PSF. $\text{SB}_{\text{cont},\nu}$ agree with null detection within 1σ uncertainties for both sample, which disfavors the UV continuum contribution to SB_{NB} .

be treated as the upper limit of $\text{SB}_{\text{cont},\nu}$. As shown in Figure 7 as an example, the values of $\text{SB}_{\text{cont},\nu}$ at $z = 2.2 - 6.6$ are consistent with null detection within $\sim (1 - 2)\sigma$ uncertainties. Additionally, we confirm that the UV continuum emission contributing to SB_{NB} , i.e., $\text{SB}_{\text{cont},\nu} \times \text{FWHM}_{\text{NB}}$, is negligible compared to SB_{NB} . Therefore, we hereafter assume that SB_{NB} is equivalent to the $\text{Ly}\alpha$ SB ($\text{SB}_{\text{Ly}\alpha}$).

In summary, we identify very diffuse ($\sim 10^{-20} - 10^{-19}$ $\text{erg s}^{-1} \text{cm}^{-2} \text{arcsec}^{-2}$) $\text{Ly}\alpha$ signals beyond R_{vir} around the *all* sample LAEs at $z = 3.3$ at the 4.1σ level. We also potentially detect positive signals around the *all* sample LAEs at $z = 5.7$ and 6.6 and *bright* subsample LAEs with $\text{S/N} \sim 2$. These results imply the potential existence of very diffuse and extended $\text{Ly}\alpha$ emission around $z = 2.2 - 6.6$ LAEs.

Again, a major update compared to Kakuma et al. (2021) is that we apply the intensity mapping technique newly to the CHORUS data to investigate extended $\text{Ly}\alpha$ emission at $z = 2.2 - 3.3$. In particular, we identify extended $\text{Ly}\alpha$ emission around the $z = 3.3$ LAEs with the S/N levels comparable or higher than those at $z = 5.7$ and 6.6 , probably thanks to the large number of LAEs at $z = 3.3$ ($N_{\text{LAE}} = 762$). Our results at $z = 5.7$ and 6.6 are consistent with those obtained in Kakuma et al. (2021), which is as expected from similar properties of the LAEs of Kakuma et al. (2021) and our *all* sample, such as N_{LAE} , the $L_{\text{Ly}\alpha}$ ranges, and the sky distributions

(Section 2.2). In the next section, we compare our results with previous work including Kakuma et al. (2021) in detail.

3.3. Comparison with Previous Work

We compare our $\text{SB}_{\text{Ly}\alpha}$ radial profiles with those of previous studies at $z \sim 2.2, 3.3, 5.7,$ and 6.6 (Figure 8). We compile the data taken from Momose et al. (2014), Momose et al. (2016), Leclercq et al. (2017), Wisotzki et al. (2018), Wu et al. (2020), and Kakuma et al. (2021), which are summarized in Table 3. Because SB is affected by the cosmological dimming effect, all the $\text{SB}_{\text{Ly}\alpha}$ profiles, including ours, are scaled by $(1+z)^{-4}$ to $z = 2.2, 3.3, 5.7,$ and 6.6 in each panel. We also shift the radii of the $\text{SB}_{\text{Ly}\alpha}$ profiles in units of ckcpc by $(1+z)$, while fixing the radii in pkpc. For our samples at $z = 5.7$ and 6.6 , we hereafter present $\text{SB}_{\text{Ly}\alpha}$ averaged at each redshift over the UD-COSMOS and UD-SXDS fields weighting by the number of LAEs in each field, unless otherwise stated.

Although the $\text{SB}_{\text{Ly}\alpha}$ profiles are measured under different seeing sizes, the typical image PSF FWHMs are as small as $\lesssim 1''.5$, corresponding to $\lesssim 40 - 60$ ckcpc at $z = 2 - 7$ (e.g. Momose et al. 2014; Ono et al. 2021). Since we focus on $\text{SB}_{\text{Ly}\alpha}$ profiles at larger scales of $\gtrsim 100$ ckcpc, PSF differences are unlikely to affect the following discussion.

Momose et al. (2016) found that $\text{SB}_{\text{Ly}\alpha}$ profiles depend on $L_{\text{Ly}\alpha}$ of the galaxy. To avoid this dependency, we take the data from Momose et al. (2014), Momose et al. (2016), and Kakuma et al. (2021), because their LAEs have $L_{\text{Ly}\alpha}$ values similar to those of our *all* samples in the same $2''$ -diameter aperture size. We additionally take the data from Leclercq et al. (2017), Wisotzki et al. (2018), and Wu et al. (2020), but these samples have different $L_{\text{Ly}\alpha}$ values measured in different aperture sizes. Therefore, for precise comparisons, we normalize the $\text{SB}_{\text{Ly}\alpha}$ profiles of these samples such that $\text{SB}_{\text{Ly}\alpha}$ integrated over a central $2''$ -diameter aperture ($= 4\pi d_L^2 \int_0^{1''} \text{SB}_{\text{Ly}\alpha}(r) \cdot 2\pi r dr$) becomes equal to $L_{\text{Ly}\alpha}$ of our *all* sample at each redshift.

The top left panel in Figure 8 presents $\text{SB}_{\text{Ly}\alpha}$ radial profiles at $z = 2.2$. We compare the results of Momose et al. (2016, $L_{\text{Ly}\alpha} = 10^{42.6}$ erg s^{-1} subsample) against our *all* sample. We found that the $\text{SB}_{\text{Ly}\alpha}$ profile of Momose et al. (2016) is in good agreement with that of our *all* sample at $r \sim 100$ ckcpc.

In the top right panel of Figure 8, we show the $\text{SB}_{\text{Ly}\alpha}$ profiles at $z = 3.3$. We compare the results of Momose et al. (2014, $z = 3.1$ LAEs), Leclercq et al. (2017, an individual LAE MUSE#106), and Wisotzki et al. (2018, $L_{\text{Ly}\alpha} > 10^{42}$ erg s^{-1} subsample at $z = 3 - 4$), and our *all* sample. The $\text{SB}_{\text{Ly}\alpha}$ profiles from the literature ap-

Table 3. Summary of the observational studies used for comparison.

Reference	z	$L_{\text{Ly}\alpha}$	Sample	Method
(1)	(2)	(3)	(4)	(5)
$z \sim 2.2$				
This Work (<i>all</i> sample)	2.2	42.5	289 LAEs	intensity mapping (mean)
Momose et al. (2016)	2.2	42.6	710 LAEs ($L_{\text{Ly}\alpha} \geq 10^{42.4} \text{ erg s}^{-1}$)	stacking (mean)
$z \sim 3.3$				
This Work (<i>all</i> sample)	3.3	42.5	762 LAEs	intensity mapping (mean)
Momose et al. (2014)	3.1	42.7	316 LAEs	stacking (mean)
Leclercq et al. (2017)	3.28	[42.5]	LAE MUSE#106*	individual detection
Wisotzki et al. (2018)	3 – 4	[42.5]	18 LAEs ($L_{\text{Ly}\alpha} > 10^{42} \text{ erg s}^{-1}$)	stacking (median)
Matsuda et al. (2012)	3.1	—	894 LAEs ($26 < BV < 27$) [†]	stacking (median)
$z \sim 5.7$				
This Work (<i>all</i> sample)	5.7	42.8	650 LAEs	intensity mapping (mean)
Momose et al. (2014)	5.7	42.7	397 LAEs	stacking (mean)
Leclercq et al. (2017)	5.98	[42.8]	LAE MUSE#547*	individual detection
Wisotzki et al. (2018)	5 – 6	[42.8]	6 LAEs ($L_{\text{Ly}\alpha} > 10^{42} \text{ erg s}^{-1}$)	stacking (median)
Wu et al. (2020)	5.7	[42.8]	310 LAEs	stacking (median)
Kakuma et al. (2021)	5.7	42.9	425 LAEs	intensity mapping (mean)
$z \sim 6.6$				
This Work (<i>all</i> sample)	6.6	43.0	80 LAEs	intensity mapping (mean)
Momose et al. (2014)	6.6	42.7	119 LAEs	stacking (mean)
Kakuma et al. (2021)	6.6	42.8	396 LAEs	intensity mapping (mean)

NOTE—Columns: (1) Reference. (2) Redshift. (3) Mean or median Ly α luminosity of the sample within a 2''-diameter aperture in units of log erg s $^{-1}$. We normalize the SB $_{\text{Ly}\alpha}$ profiles of Leclercq et al. (2017), Wisotzki et al. (2018), and Wu et al. (2020) such that SB $_{\text{Ly}\alpha}$ integrated over a central 2''-diameter aperture becomes equal to $L_{\text{Ly}\alpha}$ of our *all* sample at each redshift, which are indicated by the brackets. (4) Sample used for comparison. The parentheses indicate specific subsamples. (5) Method for deriving the SB $_{\text{Ly}\alpha}$ profiles.

* ID of the individual LAE. See Section 3.3 for the variance among the individual LAEs.

[†] $BV \equiv (2B + V)/3$, where B and V are B - and V -band magnitudes.

proximately agree with that of our *all* sample even at $r \sim R_{\text{vir}}$. We additionally show the results from a subsample of Matsuda et al. (2012) with continuum magnitudes $BV \equiv (2B + V)/3$ of $26 < BV < 27$ (typical value range for LAEs), where B and V are B - and V -band magnitudes measured with the Subaru/SC. The SB $_{\text{Ly}\alpha}$ profile of Matsuda et al. (2012) also agrees with that of our *all* sample around $r \sim R_{\text{vir}}$. We note that, although the results of Leclercq et al. (2017) are represented by their individual LAE MUSE#6905, their LAEs have similar SB $_{\text{Ly}\alpha}$ profiles when the amplitudes are normalized to match the $L_{\text{Ly}\alpha}$ values at $r \leq 1''$.

The SB $_{\text{Ly}\alpha}$ profiles at $z = 5.7$ are displayed in the bottom left panel of Figure 8. We compare the results of Momose et al. (2014, $z = 5.7$ LAEs), Leclercq et al. (2017, an individual LAE MUSE#547), Wisotzki et al.

(2018, $L_{\text{Ly}\alpha} > 10^{42} \text{ erg s}^{-1}$ subsample at $z = 5 - 6$), Wu et al. (2020, $z = 5.7$ LAEs), Kakuma et al. (2021, $z = 5.7$ LAEs), and our *all* sample. The SB $_{\text{Ly}\alpha}$ profile of our *all* sample agrees well with those of Momose et al. (2014), Leclercq et al. (2017), Wisotzki et al. (2018) and Wu et al. (2020) at $r \sim 80 - 200 \text{ ckpc}$, and with that of Kakuma et al. (2021) up to $r \sim 1 \text{ cMpc}$.

The bottom right panel of Figure 8 shows SB $_{\text{Ly}\alpha}$ profiles at $z = 6.6$ taken from Momose et al. (2014, $z = 6.6$ LAEs), Kakuma et al. (2021, $z = 6.6$ LAEs), and our *all* sample. The SB $_{\text{Ly}\alpha}$ profile of our *all* sample is consistent with those of Momose et al. (2014) and Kakuma et al. (2021) up to the scales of $r \sim 100 \text{ ckpc}$ and 1 cMpc , respectively.

In summary, our SB $_{\text{Ly}\alpha}$ profiles are in good agreement with those of the previous studies at each redshift, pro-

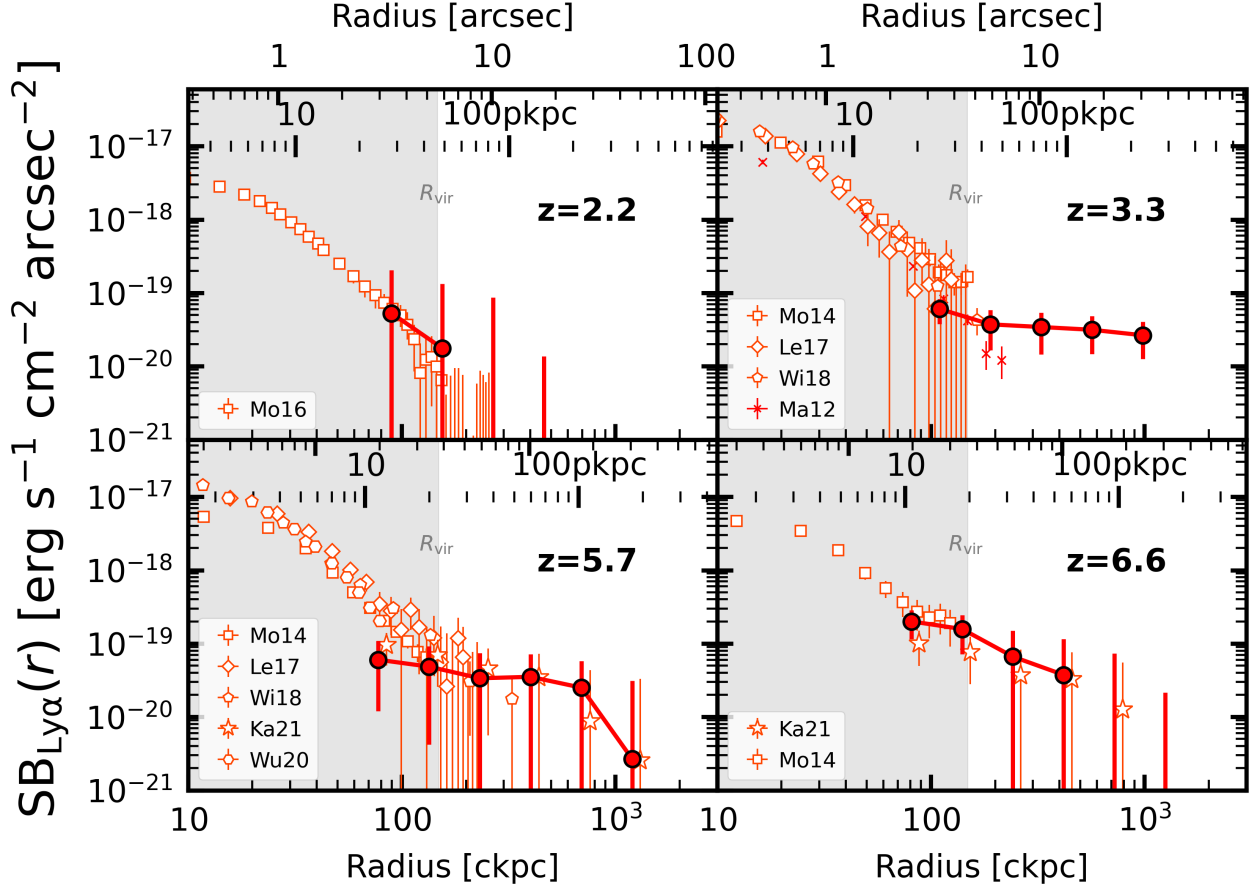


Figure 8. Comparison of the $\text{SB}_{\text{Ly}\alpha}$ radial profiles at $z = 2.2$ (top left), 3.3 (top right), 5.7 (bottom left), and 6.6 (bottom right). All the $\text{SB}_{\text{Ly}\alpha}$ profiles are corrected by $(1+z)^{-4}$ to match to each redshift. The gray shades illustrate the regions whose radius is smaller than R_{vir} of a DMH with $M_{\text{halo}} = 10^{11} M_{\odot}$. The filled red circles show the $\text{SB}_{\text{Ly}\alpha}$ profiles of our *all* sample. The profiles at $z = 5.7$ and 6.6 are averaged over the UD-COSMOS and UD-SXDS fields. The other red symbols represent the profiles taken from previous studies: Matsuda et al. (2012, Ma12: crosses), Momose et al. (2014, Mo14: squares), Momose et al. (2016, Mo16: squares), Leclercq et al. (2017, Le17: diamonds), Wisotzki et al. (2018, Wi18: pentagons), Wu et al. (2020, Wu20: hexagons), and Kakuma et al. (2021, Ka21: stars). See Table 3 for details of these samples. We omit the data points below the detection limits defined in the literature. The $\text{SB}_{\text{Ly}\alpha}$ profiles taken from Leclercq et al. (2017), Wisotzki et al. (2018), and Wu et al. (2020) are normalized such that $L_{\text{Ly}\alpha}$ values measured in a central $2''$ diameter equal to those of our *all* sample at each redshift. Some data points are slightly shifted along the horizontal axes for clarity. The $\text{SB}_{\text{Ly}\alpha}$ profiles of our *all* sample are in good agreements with those taken from the literature.

vided that the LAEs have similar $L_{\text{Ly}\alpha}$ values at $r \leq 1''$. Our $\text{SB}_{\text{Ly}\alpha}$ profiles ($r \gtrsim 80$ ckpc) are smoothly connected with the inner ($r \lesssim 100$ ckpc) profiles taken from the literature at ~ 100 ckpc, and extend to larger scales.

In Figure 9, we compare the $\text{SB}_{\text{cont},\nu}$ radial profiles between Momose et al. (2014, 2016) and our *all* sample at $z = 2.2, 3.3,$ and 5.7 (the data of Momose et al. 2014, 2016 are of the same LAEs as used in Figure 8). We find that the $\text{SB}_{\text{cont},\nu}$ profiles roughly agree at $r \lesssim 400$ ckpc, although the uncertainties are large. The $\text{SB}_{\text{cont},\nu}$ profiles are much less extended than $\text{SB}_{\text{Ly}\alpha}$ profiles, which was also suggested by Momose et al. (2014), Momose et al. (2016), and Wu et al. (2020). We note the profiles

at $z = 6.6$ are not compared here because our sample is ~ 0.3 dex brighter than that of Momose et al. (2014).

4. DISCUSSION

4.1. Redshift Evolution of Extended $\text{Ly}\alpha$ Emission Profiles

In this section, we investigate the redshift evolution of $\text{SB}_{\text{Ly}\alpha}$ profiles of extended $\text{Ly}\alpha$ emission. In Figure 10, we compare the $\text{SB}_{\text{Ly}\alpha}$ profiles of our *bright* subsamples at $z = 2.2 - 6.6$ as a function of radius in units of ckpc. We also present the results taken from Momose et al. (2014, $z = 5.7$ and 6.6 LAEs) and Wisotzki et al. (2018, $L_{\text{Ly}\alpha} > 10^{42}$ erg s^{-1} subsample at $z = 3 - 4$). Because our *bright* subsamples have uniform $L_{\text{Ly}\alpha}$ values ($\sim 10^{42.9} - 10^{43.0}$ erg s^{-1}) over $z = 2.2 - 6.6$, the

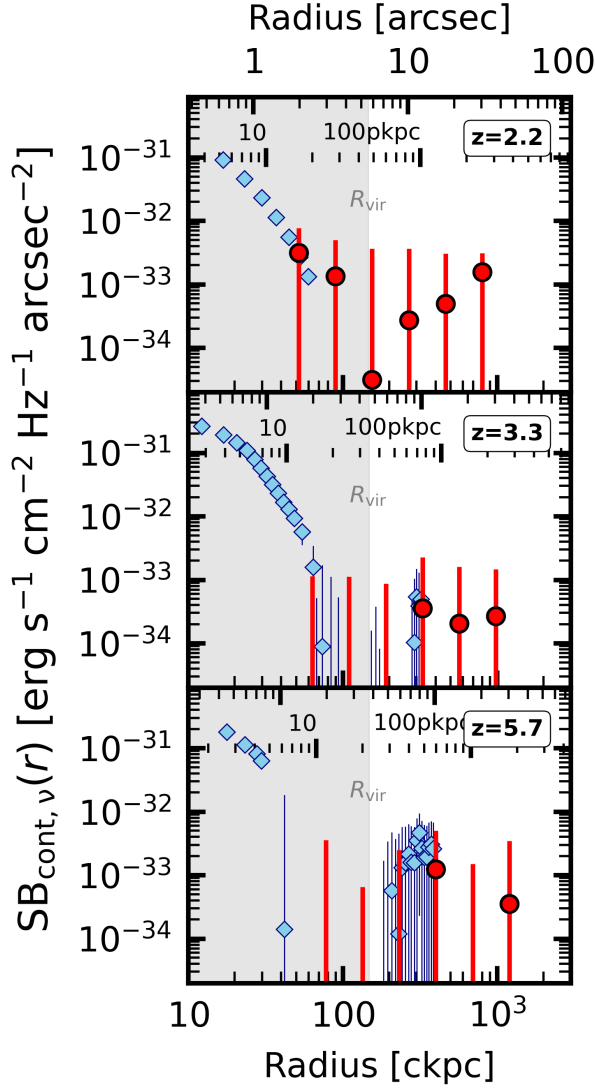


Figure 9. Comparison of the $SB_{\text{cont},\nu}$ radial profiles at $z = 2.2$ (top), 3.3 (middle), and 5.7 (bottom). The red circles and cyan diamonds show the $SB_{\text{cont},\nu}$ profiles of our *all* sample and Momose et al. (2014, 2016), respectively (we use the data of Momose et al. 2016 at $z = 2.2$, and of $z = 3.1$ and 5.7 LAEs of Momose et al. 2014 at $z = 3.3$ and 5.7 , respectively). The gray shades illustrate the regions inside R_{vir} of a DMH with $M_{\text{halo}} = 10^{11} M_{\odot}$. The $SB_{\text{cont},\nu}$ profiles of our *all* sample are in good agreements with those of Momose et al. (2014, 2016).

$L_{\text{Ly}\alpha}$ differences between the redshifts are unlikely to influence the following discussion.

The top panel of Figure 10 shows the observed $SB_{\text{Ly}\alpha}$ profiles. We identify no significant difference among the $SB_{\text{Ly}\alpha}$ profiles beyond the 1σ uncertainties at $r \sim 100 - 1000$ ckpc over $z = 2.2 - 6.6$, while the uncertainties are large. This finding is consistent with that of Kakuma et al. (2021) at $z = 5.5 - 6.6$. There is no significant difference also in the profiles at $r < 100$ ckpc, which was

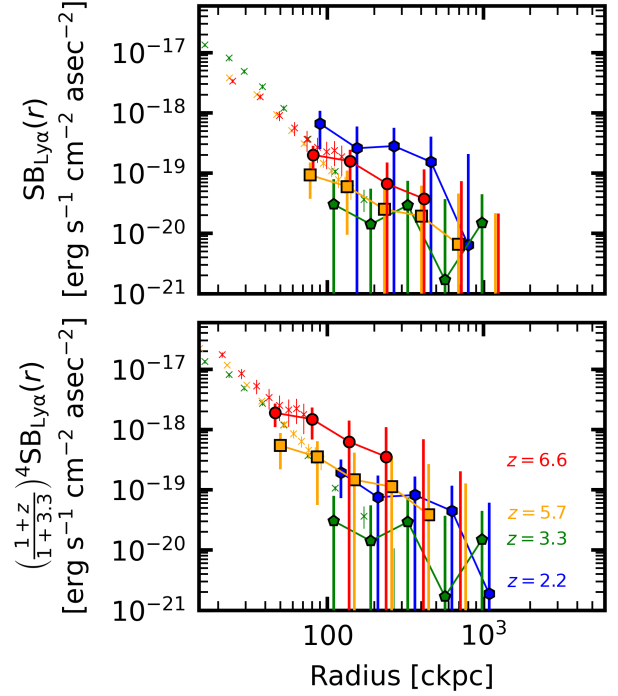


Figure 10. Comparison between $SB_{\text{Ly}\alpha}$ radial profiles at $z = 2.2 - 6.6$. **Top:** Observed $SB_{\text{Ly}\alpha}$ profiles. The blue hexagons, green pentagons, orange squares, and red circles represent the profiles of our *bright* subsamples at $z = 2.2, 3.3, 5.7,$ and 6.6 , respectively. The green, orange, and red crosses denote profiles taken from Wisotzki et al. (2018), Momose et al. (2014), and Momose et al. (2014), which are normalized to $z = 3.3, 5.7,$ and 6.6 , respectively. The $SB_{\text{Ly}\alpha}$ profile of Wisotzki et al. (2018) is normalized such that $L_{\text{Ly}\alpha}$ in $r \leq 1''$ matches to that of our *all* sample (see Section 3.3). We again note that our profiles here are based on *bright* subsamples and thus differ from those shown in Figure 8. **Bottom:** Same as the top panel, but showing the profiles corrected for the cosmological dimming effect, i.e., the intrinsic $SB_{\text{Ly}\alpha}$ profiles. We tentatively identify an increasing trend roughly by $(1+z)^3$ toward high redshifts, albeit with the large uncertainties.

also suggested by MUSE observations (Leclercq et al. 2017, see also Figure 11 of Byrohl et al. 2020) at $3 < z < 6$.

Observed $SB_{\text{Ly}\alpha}$ profiles are affected by the cosmological dimming effect. To correct this effect, we shift the observed $SB_{\text{Ly}\alpha}$ profiles vertically by $(1+z)^4/(1+3.3)^4$ and horizontally by $(1+3.3)/(1+z)$, which are hereafter termed as the *intrinsic* profiles (we match the profiles to $z = 3.3$ just for visibility). The intrinsic profiles are presented in the bottom panel of Figure 10. There is a tentative increasing trend in the intrinsic profiles toward $z = 6.6$, although those at $z = 2.2$ and 3.3 remain comparable due to the large uncertainties.

To quantitatively investigate the evolution, we derive the $\text{SB}_{\text{Ly}\alpha}$ intrinsic profiles amplitudes at $r = 200$ ckpc ($\text{SB}_{\text{Ly}\alpha, \text{intr}}$) as a function of redshift. We fit the relation with $\text{SB}_{\text{Ly}\alpha, \text{intr}} \propto (1+z)^b$, where b is a constant, weighting $\text{SB}_{\text{Ly}\alpha, \text{intr}}$ with $\sqrt{N_{\text{LAE}}}$ at each redshift. We find that the best-fit value of b is 3.1, which implies that the intrinsic $\text{SB}_{\text{Ly}\alpha}$ profile amplitudes increase toward high redshifts roughly by $(1+z)^3$ at a given radius in units of ckpc. This trend might correspond to increasing density of hydrogen gas toward high redshifts due to the evolution of the cosmic volume. Nevertheless, it is still difficult to draw a conclusion due to large uncertainties. We cannot rule out other or additional possibilities, such as higher $\text{Ly}\alpha$ escape fractions toward high redshifts (e.g., Hayes et al. 2011; Konno et al. 2016). It is also necessary to investigate potential impact of the cosmic reionization on the neutral hydrogen density at $r \sim 100 - 1000$ ckpc around LAEs. Deeper observations in the future will help to elucidate the evolution and its physical interpretation.

4.2. Physical Origins of Extended $\text{Ly}\alpha$ Emission

In this section, we compare the observational results obtained in Section 3 with theoretical models taken from the literature to investigate the mechanism of extended $\text{Ly}\alpha$ emission production. We investigate extended $\text{Ly}\alpha$ emission focusing on 1) where $\text{Ly}\alpha$ photons originate; 2) which processes produce $\text{Ly}\alpha$ photons; and 3) how these photons transfer in the surrounding materials.

1) First, we distinguish $\text{Ly}\alpha$ emission according to where it originates from:

1. The ISM of the targeted galaxy (*central galaxy*).
2. The *CGM* surrounding the central galaxy.
3. *Satellite galaxies*.
4. *Other halos*, which refer to halos distinct from that hosting the central galaxy.

2) We consider that $\text{Ly}\alpha$ photons are produced in the processes of *recombination* and/or *collisional excitation* (*cooling radiation*), as stated in the Introduction.

3) Lastly, $\text{Ly}\alpha$ photons subsequently transfer through surrounding hydrogen gas while being resonantly scattered, which affects the observed SB profiles. Hence, we should be conscious of whether models takes into account the scattering process or not (see Byrohl et al. 2020 for the impact of scattering on $\text{SB}_{\text{Ly}\alpha}$ profiles).

In Figure 11, we compare the $\text{SB}_{\text{Ly}\alpha}$ profiles that are observed (Section 3.2) and those predicted by theoretical work. The observational results are taken from Momose et al. (2016, $L_{\text{Ly}\alpha} = 10^{42.6}$ erg s^{-1} subsample at

$z = 2.2$), Wisotzki et al. (2018, $L_{\text{Ly}\alpha} > 10^{42}$ erg s^{-1} subsample at $z = 3 - 4$), Momose et al. (2014, $z = 5.7$ and 6.6 LAEs), and our *all* samples ($z = 2.2 - 6.6$). Predicted profiles are taken from Zheng et al. (2011), Dijkstra & Kramer (2012), Lake et al. (2015), Mas-Ribas et al. (2017b), Kakiichi & Dijkstra (2018), and Byrohl et al. (2020), which are summarized in Table 4. We plot these observational and theoretical results at the nearest redshifts among $z = 2.2, 3.3, 5.7,$ and 6.6 , except that the model of Mas-Ribas et al. (2017b) is presented at all the redshifts, with the correction for the cosmological dimming effect. We normalize all the profiles such that they match at $r = 1''$ in amplitude for precise comparison under the same $\text{Ly}\alpha$ luminosity of the central galaxy (the models of Zheng et al. 2011, Lake et al. 2015 and Byrohl et al. 2020 are normalized in each total profile summing up different origins). We compare these observational and theoretical results in the context of the $\text{Ly}\alpha$ photon origins in the following subsections.

4.2.1. Central Galaxy

To discuss the contribution from the *central galaxy*, we compare the models of Zheng et al. (2011), Dijkstra & Kramer (2012), Lake et al. (2015), Kakiichi & Dijkstra (2018), and Byrohl et al. (2020). They applied $\text{Ly}\alpha$ radiative transfer (RT) modeling to hydrodynamic cosmological galaxy formation simulations at $z = 5.7, 3.1, 2 - 3,$ and $2 - 5,$ respectively, to investigate $\text{Ly}\alpha$ photons produced by SF in the central galaxy and resonantly scattered into the CGM. We take the ‘one-halo’ term model from Zheng et al. (2011), where $\text{Ly}\alpha$ photons are scattered not only in the CGM but also the IGM. The model of Lake et al. (2015) takes into account the contribution from cooling radiation in addition to that from SF. The model of Kakiichi & Dijkstra (2018) is taken in an approximated form of their Equation (28). The model of Byrohl et al. (2020) considers recombination caused by ionizing photons from SF and UVB as well as cooling via collisional de-excitation.

The black lines in Figure 11 represent the contribution from the central galaxy: Kakiichi & Dijkstra (2018, dotted, $z = 2.2$), Byrohl et al. (2020, solid, $z = 3.3$), Lake et al. (2015, dash-dotted, $z = 3.3$), Dijkstra & Kramer (2012, dotted, $z = 3.3$), and Zheng et al. (2011, dotted, $z = 5.7$). These models successfully reproduce the observed $\text{SB}_{\text{Ly}\alpha}$ profiles inside the CGM ($r < R_{\text{vir}}$) at $z = 3.3$ and 5.7 , implying resonant scattering as a major source powering $\text{Ly}\alpha$ emission. This finding is also supported by previous studies in other aspects, such as halo properties (e.g., a halo luminosity-mass relation; Kusakabe et al. 2019) and kinematics (e.g., a correlation between the peak velocity shift and the width of a

Table 4. Summary of the theoretical studies used for comparison.

Reference	z_{model}	z_{plot}	Origin	Process	Scattering	$M_{\text{halo}} (M_{\odot})$
(1)	(2)	(3)	(4)	(5)	(6)	(7)
Mas-Ribas et al. (2017b)	5.7, 6.6	2.2, 3.3, 5.7, 6.6	CGM/Sat.	Rec.	n	10^{11} *
Kakiichi & Dijkstra (2018)	2 – 3	2.2	Cen.	Rec.	y	$\sim 10^{12}$
Byrohl et al. (2020)	2 – 5	3.3	Cen./Sat./Other.	Rec./Cool.	y	$\sim 10^{11}$ #
Dijkstra & Kramer (2012)	~ 2.65	3.3	Cen.	Rec.	y	—
Lake et al. (2015)	3.1	3.3	Cen./Other.	Rec./Cool.	y	$10^{11.5}$
Zheng et al. (2011)	5.7	5.7	Cen./Other.	Rec.	y	$10^{11.2}$

NOTE—Columns: (1) Reference. (2) Redshift assumed in the model. (3) Redshift where we plot the model in Figure 11. (4) Origins of Ly α photons (where Ly α photons are produced): the central galaxy (Cen.), CGM, satellite galaxies (Sat.), and other halos (Other.) (5) Physical processes of Ly α emission production (how Ly α emission is produced): recombination (Rec.), and cooling radiation (Cool.). (6) Whether the model takes into account Ly α RT (i.e., resonant scattering) or not. (7) Assumed halo mass in units of M_{\odot} .

* We fix M_{halo} to $10^{11} M_{\odot}$, while M_{halo} is a free parameter in the model.

This value was converted from the assumed stellar mass M_{\star} of $10^{8.5} - 10^{9.5} M_{\odot}$ with the $M_{\star}/M_{\text{halo}}$ ratio obtained in Behroozi et al. (2019).

Ly α line, Leclercq et al. 2020; red peak dominated Ly α spectra, Chen et al. 2021).

The one-halo term of Zheng et al. (2011) reproduces the observed SB_{Ly α} profile also from $r \sim R_{\text{vir}}$ up to ~ 1 cMpc at $z = 5.7$. They considered resonant scattering in the IGM in addition to the CGM. This effect leads to a plateau-like feature in a SB_{Ly α} profile at $r \sim 0.3 - 1$ cMpc (see also Jeesson-Daniel et al. 2012), which is similar to those at $z = 3.3$ and 5.7 . Therefore, we may interpret that the observed extended Ly α emission outside the CGM is produced by resonant scattering in the IGM, although the uncertainties are large. At $z = 3.3$, however, the models adopted here (Lake et al. 2015, Dijkstra & Kramer 2012, and Byrohl et al. 2020) produce values lying far below the observed SB_{Ly α} profile beyond 300 ckpc and do not reproduce a plateau-like shape, unlike the one-halo term of Zheng et al. (2011). One possibility is that the contribution from the central galaxy decreases from $z = 5.7$ to 3.3 , but there is no evidence to confirm this. Alternatively, we suppose that this discrepancy can be attributed to the different assumptions and incorporated physics in the models, such as treatment of stellar radiation, dusts, and scattering, especially beyond R_{vir} . Nevertheless, since the one-halo term of Zheng et al. (2011) reproduces the observed SB_{Ly α} profile at $z = 5.7$, we cannot rule out the possibility that scattered Ly α photons originating from the central galaxy contribute to extended Ly α emission beyond R_{vir} . We need additional inputs on the neutral hydrogen gas distribution outside R_{vir} to further determine the contribution of resonant scattering.

The assumptions on M_{halo} values are unlikely to affect our discussion here, because the models above use roughly similar M_{halo} values: $10^{11.2}$ and $10^{11.5} M_{\odot}$ for Zheng et al. (2011) and Lake et al. (2015), respectively. Byrohl et al. (2020) assume a stellar mass M_{\star} range of $10^{8.5} - 10^{9.5} M_{\odot}$ at $z = 3$, which corresponds to $M_{\text{halo}} \sim 10^{11} M_{\odot}$ given the $M_{\star}/M_{\text{halo}}$ ratio obtained in Behroozi et al. (2019, see also Kusakabe et al. 2018). These values are similar to those obtained in the previous observations (e.g., Ouchi et al. 2010; Kusakabe et al. 2018).

4.2.2. CGM

We next use the model from Mas-Ribas et al. (2017b) to investigate the Ly α emission produced in the CGM. They constructed an analytical model of fluorescent emission in the CGM caused by ionizing radiation from SF in the central galaxy at $z = 5.7$ and 6.6 (we apply this model also to $z = 3.3$ and 2.2 ; see also Mas-Ribas & Dijkstra 2016). The model of Mas-Ribas et al. (2017b) includes three free parameters: 1) the CGM structure, 2) SF rate (SFR), and 3) radius R_{max} . 1) We adopt the simplified clumpy outflow model of Steidel et al. (2010) as the CGM structure (the choice here has only a small impact on SB_{Ly α} profiles; see Figure 2 of Mas-Ribas & Dijkstra 2016). 2) We normalize the model with SFR = 1, 10, 10, and 20 $M_{\odot} \text{ yr}^{-1}$ at $z = 2.2, 3.3, 5.7, 6.6$, respectively. 3) SB_{Ly α} (b) is derived as the integration of Ly α emissivity at radius r over $b \leq r \leq R_{\text{max}}$, where b denotes the impact parameter (see Equations 4 and 2 of Mas-Ribas & Dijkstra 2016 and Mas-Ribas

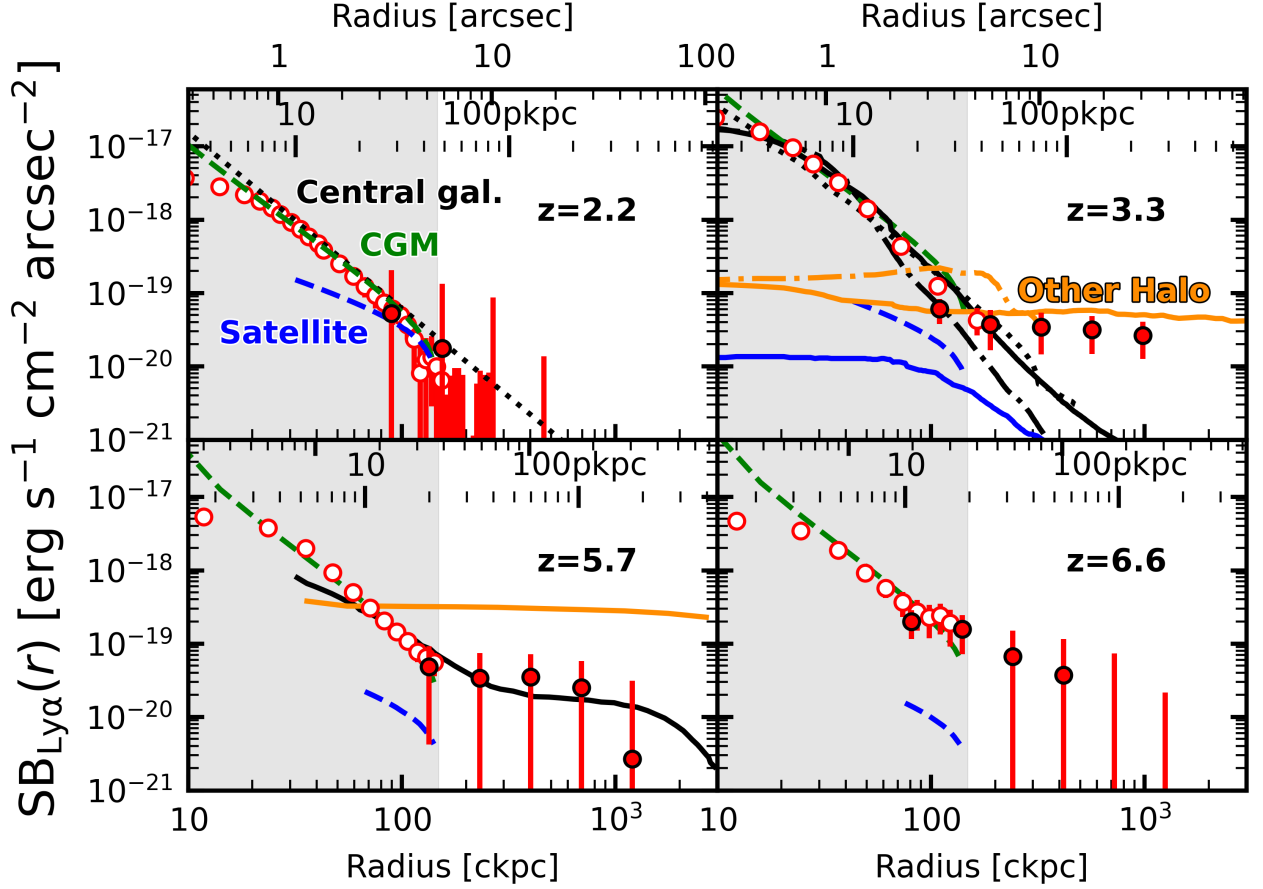


Figure 11. Comparison of the $\text{SB}_{\text{Ly}\alpha}$ radial profiles between the observational and theoretical studies at $z = 2.2$ (top left), 3.3 (top right), 5.7 (bottom left), and 6.6 (bottom right). The filled red circles depict the observational results taken from our *all* sample ($z = 2.2 - 6.6$), while the open red circles show the results from previous observational work (Momose et al. 2016 at $z = 2.2$, Wisotzki et al. 2018 at $z = 3.3$, and Momose et al. 2014 at $z = 5.7$ and 6.6). The $\text{SB}_{\text{Ly}\alpha}$ amplitude of Wisotzki et al. (2018) is normalized such that $L_{\text{Ly}\alpha}$ in $r \leq 1''$ matches to that of our *all* sample (see Section 3.3). We represent the theoretical work with the lines, whose colors indicate the $\text{Ly}\alpha$ emission origins: the central galaxy (black), CGM (green), satellite galaxies (blue), and other halos (orange). The models are taken from Mas-Ribas et al. (2017b, green and blue dashed lines at $z = 2.2, 3.3, 5.7, 6.6$), Kakiichi & Dijkstra (2018, black dotted line at $z = 2.2$), Byrohl et al. (2020, black, blue, and orange solid lines at $z = 3.3$), Lake et al. (2015, black and orange dash-dotted lines at $z = 3.3$), Dijkstra & Kramer (2012, black dotted line at $z = 3.3$), and Zheng et al. (2011, black and orange solid lines at $z = 5.7$). See Table 4 for details of these models. We normalize the $\text{SB}_{\text{Ly}\alpha}$ profiles from the model predictions such that the central galaxy ($r \leq 1''$) has the $L_{\text{Ly}\alpha}$ value similar to that observed at each redshift. The gray shades illustrate the regions inside R_{vir} of a DMH with $M_{\text{halo}} = 10^{11} M_{\odot}$.

et al. 2017b, respectively). Here R_{max} represents the extent to which $\text{Ly}\alpha$ emission contributes to $\text{SB}_{\text{Ly}\alpha}$. We assume that R_{max} is equivalent to R_{vir} for a DMH of $M_{\text{halo}} = 10^{11} M_{\odot}$ ($= 46, 34, 22,$ and 20 pkpc at $z = 2.2, 3.3, 5.7,$ and 6.6 , respectively). Their model ignores the effect of resonant scattering.

The green dashed lines in Figure 11 represent the model of Mas-Ribas et al. (2017b). The $\text{SB}_{\text{Ly}\alpha}$ profiles predicted by their model are in good agreement with those observed inside R_{vir} at all the redshifts. However, because $\text{SB}_{\text{Ly}\alpha}$ profiles drops sharply at $r = R_{\text{max}}$ according to this model, the emission originating from the CGM cannot contribute to extended emission beyond R_{vir} . Mas-Ribas & Dijkstra (2016) and Mas-Ribas

et al. (2017b) arbitrarily adopted much larger R_{max} values (> 100 pkpc) to reproduce the profiles obtained in Momose et al. (2014), but such large R_{max} values correspond to $M_{\text{halo}} > 10^{12} M_{\odot}$, which is much larger than those observed (e.g., Ouchi et al. 2010; Kusakabe et al. 2018). If R_{max} is larger than R_{vir} , materials should exist outside the CGM ($\gtrsim 3$ times larger scales than R_{vir}) and produce fluorescent emission contributing to extended $\text{Ly}\alpha$ emission. In either case, the observed $\text{SB}_{\text{Ly}\alpha}$ profiles beyond 300 cpkc at $z = 3.3$ cannot be reproduced even with larger values of R_{max} .

Overall, fluorescence in the CGM can power $\text{Ly}\alpha$ emission inside R_{vir} according to the model of Mas-Ribas et al. (2017b), while it plays only a marginal role beyond

R_{vir} . This behavior was also suggested by MUSE UDF data (Gallego et al. 2018; Bacon et al. 2021). We note that the model of Mas-Ribas et al. (2017b) ignores the scattering effect, which leads to a sharp drop of $\text{SB}_{\text{Ly}\alpha}$ at $r = R_{\text{max}}$. Hence, it is necessary to incorporate resonant scattering to extend Ly α emission when we rely on the CGM fluorescence scenario.

The contribution from cooling radiation in the CGM remains unclear. Byrohl et al. (2020) argued that cooling radiation dominates $\sim 30\%$ of the total Ly α emission at $r \gtrsim 20$ pkpc. On the other hand, Rosdahl & Blaizot (2012) found that Ly α emission from cooling radiation is centrally ($r < 10$ pkpc) concentrated for a DMH with $M_{\text{halo}} = 10^{11} M_{\odot}$. We need additional models at larger scales to further discuss whether cooling radiation contributes to extended Ly α emission or not.

4.2.3. Satellite Galaxies

We adopt another model from Mas-Ribas et al. (2017b), which predicts the contribution from SF in *satellite galaxies* (see also Mas-Ribas et al. 2017a). There are three free parameters in their model: 1) a clustering description, 2) Ly α escape fraction ($f_{\text{Ly}\alpha}^{\text{esc}}$), and 3) R_{max} . 1) We assume that clustering follows a power-law two-point cross-correlation function $\xi(r)$ of $\xi(r) = (r/r_0)^{-\alpha}$ with the scale length $r_0 = 4$ cMpc and index $\alpha = 1.8$ (e.g., Ouchi et al. 2010; Harikane et al. 2016; Bielby et al. 2017). 2) We fix $f_{\text{Ly}\alpha}^{\text{esc}}$ to 0.4, while $\text{SB}_{\text{Ly}\alpha}$ linearly depends on $f_{\text{Ly}\alpha}^{\text{esc}}$. 3) Satellite galaxies are assumed to exist from $r = 10$ pkpc to R_{max} , which we assume equal to R_{vir} in the same way as for the fluorescence model (Section 4.2.2). We additionally take the ‘outer halo’ model from Byrohl et al. (2020).

The blue dashed and solid lines represent the models of Mas-Ribas et al. (2017b) and Byrohl et al. (2020), respectively. We find that the contribution from satellite galaxies are negligible compared to the other contributions, except at $r \sim 100$ ckpc at $z = 2.2$. While we choose a power-law correlation function to describe the clustering, other choices, such as the Navarro-Frenk-White (NFW) profile (Navarro et al. 1997), reduce the $\text{SB}_{\text{Ly}\alpha}$ values at $r > 40$ ckpc (see the left panel of Figure 2 of Mas-Ribas et al. 2017a). When a power-law correlation function is assumed, larger r_0 values increase the overall profiles. However, unrealistically large values of r_0 and R_{max} are necessary to reproduce extended Ly α emission beyond R_{vir} with satellite galaxies alone. Additionally, the model overpredicts the observed $\text{SB}_{\text{cont},\nu}$ values when the model is tuned to reproduce the observed $\text{SB}_{\text{Ly}\alpha}$ profiles (Mas-Ribas et al. 2017a).

For these reasons, we conclude that satellite galaxies are unlikely to contribute to extended Ly α emission be-

yond R_{vir} . This conclusion is supported by the fact that emission is more extended in Ly α than in UV continuum (Section 3.2; see also Momose et al. 2014, 2016; Wu et al. 2020), because the $\text{SB}_{\text{cont},\nu}$ profiles should be extended similarly as the $\text{SB}_{\text{Ly}\alpha}$ profiles if satellite galaxies contribute to $\text{SB}_{\text{Ly}\alpha}$.

4.2.4. Other Halos

Lastly, we compare the models for *other halos* taken from Zheng et al. (2011), Lake et al. (2015), and Byrohl et al. (2020). From Lake et al. (2015) we specifically adopt the model in which Ly α emission originates from ‘knots,’ the regions with high Ly α emissivity around the central galaxy. The ‘two-halo’ term model is taken from Zheng et al. (2011).

We show these models with the orange lines in Figure 11: Byrohl et al. (2020, solid, $z = 3.3$), Lake et al. (2015, dash-dotted, $z = 3.3$), and Zheng et al. (2011, solid, $z = 5.7$). At $z = 3.3$, the contribution from other halos predicted by Byrohl et al. (2020) agrees with the observed $\text{SB}_{\text{Ly}\alpha}$ profiles within the 1σ uncertainties. Although the knots model of Lake et al. (2015) is limited to $r \lesssim 300$ ckpc, it roughly reproduces the observed profiles at $r \sim (200 - 300)$ ckpc. On the other hand, the two-halo term of Zheng et al. (2011) at $z = 5.7$ significantly overestimates the $\text{SB}_{\text{Ly}\alpha}$ values beyond 100 ckpc. The amplitudes of the models of Zheng et al. (2011) and Byrohl et al. (2020) differ by ~ 1 dex, similarly as we found in Section 4.2.1.

Kakuma et al. (2021) argued that the difference is caused because they masked out bright objects. However, this interpretation is not necessarily appropriate, since the profile of Byrohl et al. (2020) has an amplitude similar to (or rather slightly higher than) profiles observed at $z = 3.3$. The two-halo term of Zheng et al. (2011) also overpredicts the $\text{SB}_{\text{Ly}\alpha}$ values of Momose et al. (2014). Nevertheless, we cannot rule out the possibility that other halos contribute to extended Ly α emission beyond R_{vir} , since the model of Byrohl et al. (2020) agrees with the observed $\text{SB}_{\text{Ly}\alpha}$ profiles. This suggestion is consistent with Bacon et al. (2021), who identified very extended (> 300 arcsec² or $> 2 \times 10^4$ pkpc²) Ly α emission at $z \sim 3$ using MUSE data; they found that 70% of the total Ly α luminosity originates from filamentary structures beyond the CGM. They argued that the extended Ly α emission can be reproduced by a population of extremely faint ($< 10^{40}$ erg s⁻¹) galaxies under certain conditions, which correspond to other halos considered in this subsection.

We note that the $\text{SB}_{\text{Ly}\alpha}$ profile of our *all* sample at $z = 5.7$ increases when we use only LAEs in the UDCOSMOS field, resulting in a smaller amplitude gap be-

tween the two-halo term of Zheng et al. (2011) and our profile. However, our profile based solely on the UD-COSMOS field disagrees with those from the previous observational studies. We thus suppose that the averaged profile is more appropriate for comparison against the models.

4.2.5. Overall Interpretation

In summary, $\text{SB}_{\text{Ly}\alpha}$ profiles inside the CGM ($< R_{\text{vir}}$) are possibly explained either by scattered $\text{Ly}\alpha$ emission originating from the central galaxy and/or fluorescent emission in the CGM. Meanwhile, extended $\text{Ly}\alpha$ emission beyond R_{vir} is possibly powered either by resonant scattering at large scales and/or contributed from other halos. Fluorescence in the CGM and satellite galaxies are not sufficient to reproduce the observed $\text{SB}_{\text{Ly}\alpha}$ profiles beyond R_{vir} .

We emphasize that the processes and origins of $\text{Ly}\alpha$ emission may differ among LAEs. They may also vary according to radius and redshift even when we focus on averaged profiles around different LAEs. However, our systematic investigation of extended $\text{Ly}\alpha$ emission at $z = 2 - 7$ is advantageous for a comprehensive understanding of the processes and origins of extended $\text{Ly}\alpha$ emission. More simulations focusing on large scales will help to further distinguish the processes and origins.

5. SUMMARY

In this paper, we investigated very extended $\text{Ly}\alpha$ emission around LAEs at $z = 2.2 - 6.6$ by applying the intensity mapping technique to the Subaru/HSC-SSP and CHORUS data. Our major findings are summarized below:

1. We calculated cross-correlation functions between 1781 LAEs at $z = 2.2, 3.3, 5.7$ and 6.6 with $\text{Ly}\alpha$ emission traced by the NB387, NB527, NB816, and NB921 images. A total of $\sim 1 - 2$ billion pixels were used to derive the correlation function for each redshift. The deep ($m_{\text{NB},5\sigma} \sim 26$ mag) and wide ($\sim 4 \text{ deg}^2$ over the UD-COSMOS and UD-SXDS fields) images of the HSC enabled us to detect very diffuse $\text{Ly}\alpha$ emission. We utilized foreground objects (NonLAEs) to carefully estimate the systematics, including the sky background and PSF. Subtracting these systematics, we identified the $\text{Ly}\alpha$ emission of $\sim 10^{-20} - 10^{-19} \text{ erg s}^{-1} \text{ cm}^{-2} \text{ arcsec}^{-2}$ with $\text{S/N} = 4.1$ around the $z = 3.3$ LAEs. $\text{Ly}\alpha$ emission extends beyond the radial scale of the R_{vir} of a DMH with $10^{11} M_{\odot}$ ($\sim 100 \text{ ckpc}$), and up to $\sim 1 \text{ cMpc}$. We also tentatively detected $\text{Ly}\alpha$ emission beyond the R_{vir}

scales at $z = 5.7$, and 6.6 with $\text{S/N} \sim 2$. Extended $\text{Ly}\alpha$ emission was also tentatively detected around the $z = 2.2$ LAEs when faint LAEs were excluded from the sample.

2. We confirmed that the $\text{Ly}\alpha$ surface brightness ($\text{SB}_{\text{Ly}\alpha}$) radial profiles around our LAEs agree well with those obtained in the previous studies, when the LAEs have similar $\text{Ly}\alpha$ luminosity values.
3. We compared the observed $\text{SB}_{\text{Ly}\alpha}$ profiles across $z = 2.2 - 6.6$, finding no significant difference among the redshifts beyond the uncertainties. Meanwhile, there is a potential increasing trend toward high redshifts in the *intrinsic* $\text{SB}_{\text{Ly}\alpha}$ profiles, which are corrected for the cosmological dimming effect. The increasing trend roughly follows $(1+z)^3$, which might be explained by the increasing density of the neutral hydrogen gas due to the evolution of the cosmic volume.
4. We compared the $\text{SB}_{\text{Ly}\alpha}$ profiles obtained from the observational and theoretical studies. We found that the observed $\text{SB}_{\text{Ly}\alpha}$ profiles inside the CGM can be reproduced by the models in which $\text{Ly}\alpha$ photons originating from the central galaxy subsequently transfer into the CGM via resonant scattering, or in which $\text{Ly}\alpha$ emission is produced in the CGM via fluorescence due to ionizing photons. Extended $\text{Ly}\alpha$ emission beyond R_{vir} may be reproduced by resonant scattering at large scales, and/or emission originating from clustered halos around the targeted galaxy. The CGM and satellite galaxies are unlikely to contribute to extended $\text{Ly}\alpha$ emission beyond R_{vir} .

This work, in conjunction with the previous observational studies, might suggest that very extended diffuse $\text{Ly}\alpha$ emission beyond R_{vir} ubiquitously exist around LAEs at $z \sim 2 - 7$, not only around massive galaxies. Deeper images obtained by larger-area surveys in the future should enable further investigation of very extended $\text{Ly}\alpha$ emission at more diffuse levels. Applying the intensity mapping technique to the emission of multiple lines, such as $\text{H}\alpha$ and $[\text{OIII}]$, will help to further distinguish physical processes and origins of extended $\text{Ly}\alpha$ emission, because they trace different components (see Figures 6 and 12 of Mas-Ribas et al. 2017a and Fujimoto et al. 2019). These emission lines will be observed with next-generation facilities, such as the James-Webb Space Telescope (JWST), the Nancy Grace Roman Space Telescope (NGRST), and Spectro-Photometer for the History of the Universe, Epoch of Reionization and Ices Explorer (SPHEREx).

ACKNOWLEDGEMENTS

We are grateful to Chris Byrohl for helpful comments and discussions especially on simulations and physical interpretations.

The HSC collaboration includes the astronomical communities of Japan and Taiwan, and Princeton University. The HSC instrumentation and software were developed by the National Astronomical Observatory of Japan (NAOJ), the Kavli Institute for the Physics and Mathematics of the Universe (Kavli IPMU), the University of Tokyo, the High Energy Accelerator Research Organization (KEK), the Academia Sinica Institute for Astronomy and Astrophysics in Taiwan (ASIAA), and Princeton University. Funding was contributed by the FIRST program from the Japanese Cabinet Office, the Ministry of Education, Culture, Sports, Science and Technology (MEXT), the Japan Society for the Promotion of Science (JSPS), Japan Science and Technology Agency (JST), the Toray Science Foundation, NAOJ, Kavli IPMU, KEK, ASIAA, and Princeton University.

The Pan-STARRS1 Surveys (PS1) and the PS1 public science archive have been made possible through contributions by the Institute for Astronomy, the University of Hawaii, the Pan-STARRS Project Office, the Max Planck Society and its participating institutes, the Max Planck Institute for Astronomy, Heidelberg, and the Max Planck Institute for Extraterrestrial Physics, Garching, The Johns Hopkins University, Durham University, the University of Edinburgh, the Queen's University Belfast, the Harvard-Smithsonian Center for Astrophysics, the Las Cumbres Observatory Global Telescope Network Incorporated, the National Central University of Taiwan, the Space Telescope Science Institute, the National Aeronautics and Space Administration under grant No. NNX08AR22G issued through the Planetary Science Division of the NASA Science Mission Di-

rectorate, the National Science Foundation grant No. AST-1238877, the University of Maryland, Eotvos Lorand University (ELTE), the Los Alamos National Laboratory, and the Gordon and Betty Moore Foundation.

This paper makes use of software developed for the Large Synoptic Survey Telescope. We thank the LSST Project for making their code available as free software at <http://dm.lsst.org>.

This paper is based on data collected at the Subaru Telescope and retrieved from the HSC data archive system, which is operated by the Subaru Telescope and Astronomy Data Center (ADC) at National Astronomical Observatory of Japan. Data analysis was in part carried out with the cooperation of Center for Computational Astrophysics (CfCA), National Astronomical Observatory of Japan. The Subaru Telescope is honored and grateful for the opportunity of observing the Universe from Maunakea, which has the cultural, historical and natural significance in Hawaii.

The NB387 filter was supported by KAKENHI (23244022) Grant-in-Aid for Scientific Research (A) through the JSPS. The NB527 filter was supported by KAKENHI (24244018) Grant-in-Aid for Scientific Research (A) through the JSPS. The NB816 filter was supported by Ehime University. The NB921 filter was supported by KAKENHI (23244025) Grant-in-Aid for Scientific Research (A) through the JSPS.

This work is supported by the World Premier International Research Center Initiative (WPI Initiative), MEXT, Japan, as well as KAKENHI Grant-in-Aid for Scientific Research (A) (20H00180, and 21H04467) through the JSPS. This work was supported by JSPS KAKENHI Grant Numbers 17H01114, 19J01222, 20J11993, and 21K13953.

This work was supported by the joint research program of the Institute for Cosmic Ray Research (ICRR), University of Tokyo.

REFERENCES

- Aihara, H., AlSayyad, Y., Ando, M., et al. 2019, PASJ, 71, 114, doi: [10.1093/pasj/psz103](https://doi.org/10.1093/pasj/psz103)
- Arrigoni Battaia, F., Hennawi, J. F., Prochaska, J. X., et al. 2019, MNRAS, 482, 3162, doi: [10.1093/mnras/sty2827](https://doi.org/10.1093/mnras/sty2827)
- Bacon, R., Mary, D., Garel, T., et al. 2021, A&A, 647, A107, doi: [10.1051/0004-6361/202039887](https://doi.org/10.1051/0004-6361/202039887)
- Behroozi, P., Wechsler, R. H., Hearin, A. P., & Conroy, C. 2019, MNRAS, 488, 3143, doi: [10.1093/mnras/stz1182](https://doi.org/10.1093/mnras/stz1182)
- Bertin, E., & Arnouts, S. 1996, A&AS, 117, 393, doi: [10.1051/aas:1996164](https://doi.org/10.1051/aas:1996164)
- Bielby, R. M., Shanks, T., Crighton, N. H. M., et al. 2017, MNRAS, 471, 2174, doi: [10.1093/mnras/stx1772](https://doi.org/10.1093/mnras/stx1772)
- Bond, N. A., Feldmeier, J. J., Matković, A., et al. 2010, ApJL, 716, L200, doi: [10.1088/2041-8205/716/2/L200](https://doi.org/10.1088/2041-8205/716/2/L200)
- Borisova, E., Cantalupo, S., Lilly, S. J., et al. 2016, ApJ, 831, 39, doi: [10.3847/0004-637X/831/1/39](https://doi.org/10.3847/0004-637X/831/1/39)
- Bosch, J., Armstrong, R., Bickerton, S., et al. 2018, PASJ, 70, S5, doi: [10.1093/pasj/psx080](https://doi.org/10.1093/pasj/psx080)
- Byrohl, C., Nelson, D., Behrens, C., et al. 2020, arXiv e-prints, arXiv:2009.07283, <https://arxiv.org/abs/2009.07283>
- Cantalupo, S., Arrigoni-Battaia, F., Prochaska, J. X., Hennawi, J. F., & Madau, P. 2014, Nature, 506, 63, doi: [10.1038/nature12898](https://doi.org/10.1038/nature12898)

- Cantalupo, S., Porciani, C., Lilly, S. J., & Miniati, F. 2005, *ApJ*, 628, 61, doi: [10.1086/430758](https://doi.org/10.1086/430758)
- Carilli, C. L. 2011, *ApJL*, 730, L30, doi: [10.1088/2041-8205/730/2/L30](https://doi.org/10.1088/2041-8205/730/2/L30)
- Chen, Y., Steidel, C. C., Erb, D. K., et al. 2021, arXiv e-prints, arXiv:2104.10173, <https://arxiv.org/abs/2104.10173>
- Claeysens, A., Richard, J., Blaizot, J., et al. 2019, *MNRAS*, 489, 5022, doi: [10.1093/mnras/stz2492](https://doi.org/10.1093/mnras/stz2492)
- Comaschi, P., & Ferrara, A. 2016a, *MNRAS*, 455, 725, doi: [10.1093/mnras/stv2339](https://doi.org/10.1093/mnras/stv2339)
- . 2016b, *MNRAS*, 463, 3078, doi: [10.1093/mnras/stw2199](https://doi.org/10.1093/mnras/stw2199)
- Croft, R. A. C., Miralda-Escudé, J., Zheng, Z., Blomqvist, M., & Pieri, M. 2018, *MNRAS*, 481, 1320, doi: [10.1093/mnras/sty2302](https://doi.org/10.1093/mnras/sty2302)
- Croft, R. A. C., Miralda-Escudé, J., Zheng, Z., et al. 2016, *MNRAS*, 457, 3541, doi: [10.1093/mnras/stw204](https://doi.org/10.1093/mnras/stw204)
- Dawson, K. S., Schlegel, D. J., Ahn, C. P., et al. 2013, *AJ*, 145, 10, doi: [10.1088/0004-6256/145/1/10](https://doi.org/10.1088/0004-6256/145/1/10)
- Dijkstra, M., & Kramer, R. 2012, *MNRAS*, 424, 1672, doi: [10.1111/j.1365-2966.2012.21131.x](https://doi.org/10.1111/j.1365-2966.2012.21131.x)
- Eisenstein, D. J., Weinberg, D. H., Agol, E., et al. 2011, *AJ*, 142, 72, doi: [10.1088/0004-6256/142/3/72](https://doi.org/10.1088/0004-6256/142/3/72)
- Fardal, M. A., Katz, N., Gardner, J. P., et al. 2001, *ApJ*, 562, 605, doi: [10.1086/323519](https://doi.org/10.1086/323519)
- Faucher-Giguère, C.-A., Kereš, D., Dijkstra, M., Hernquist, L., & Zaldarriaga, M. 2010, *ApJ*, 725, 633, doi: [10.1088/0004-637X/725/1/633](https://doi.org/10.1088/0004-637X/725/1/633)
- Feldmeier, J. J., Hagen, A., Ciardullo, R., et al. 2013, *ApJ*, 776, 75, doi: [10.1088/0004-637X/776/2/75](https://doi.org/10.1088/0004-637X/776/2/75)
- Fisher, Ronald Aylmer, S. 1970, *Statistical methods for research workers*, 14th edn. (Edinburgh : Oliver and Boyd)
- Fonseca, J., Silva, M. B., Santos, M. G., & Cooray, A. 2017, *MNRAS*, 464, 1948, doi: [10.1093/mnras/stw2470](https://doi.org/10.1093/mnras/stw2470)
- Fujimoto, S., Ouchi, M., Ferrara, A., et al. 2019, *ApJ*, 887, 107, doi: [10.3847/1538-4357/ab480f](https://doi.org/10.3847/1538-4357/ab480f)
- Furlanetto, S. R., Schaye, J., Springel, V., & Hernquist, L. 2005, *ApJ*, 622, 7, doi: [10.1086/426808](https://doi.org/10.1086/426808)
- Gallego, S. G., Cantalupo, S., Lilly, S., et al. 2018, *MNRAS*, 475, 3854, doi: [10.1093/mnras/sty037](https://doi.org/10.1093/mnras/sty037)
- Garel, T., Blaizot, J., Rosdahl, J., et al. 2021, *MNRAS*, 504, 1902, doi: [10.1093/mnras/stab990](https://doi.org/10.1093/mnras/stab990)
- Goerdt, T., Dekel, A., Sternberg, A., et al. 2010, *MNRAS*, 407, 613, doi: [10.1111/j.1365-2966.2010.16941.x](https://doi.org/10.1111/j.1365-2966.2010.16941.x)
- Gong, Y., Cooray, A., Silva, M. B., Santos, M. G., & Lubin, P. 2011, *ApJL*, 728, L46, doi: [10.1088/2041-8205/728/2/L46](https://doi.org/10.1088/2041-8205/728/2/L46)
- Goto, T., Utsumi, Y., Furusawa, H., Miyazaki, S., & Komiyama, Y. 2009, *MNRAS*, 400, 843, doi: [10.1111/j.1365-2966.2009.15486.x](https://doi.org/10.1111/j.1365-2966.2009.15486.x)
- Haiman, Z., Spaans, M., & Quataert, E. 2000, *ApJL*, 537, L5, doi: [10.1086/312754](https://doi.org/10.1086/312754)
- Harikane, Y., Ouchi, M., Ono, Y., et al. 2016, *ApJ*, 821, 123, doi: [10.3847/0004-637X/821/2/123](https://doi.org/10.3847/0004-637X/821/2/123)
- Harikane, Y., Ouchi, M., Shibuya, T., et al. 2018, *ApJ*, 859, 84, doi: [10.3847/1538-4357/aabd80](https://doi.org/10.3847/1538-4357/aabd80)
- Harikane, Y., Ouchi, M., Ono, Y., et al. 2019, *ApJ*, 883, 142, doi: [10.3847/1538-4357/ab2cd5](https://doi.org/10.3847/1538-4357/ab2cd5)
- Hayashi, M., Shimakawa, R., Tanaka, M., et al. 2020, *PASJ*, 72, 86, doi: [10.1093/pasj/psaa076](https://doi.org/10.1093/pasj/psaa076)
- Hayashino, T., Matsuda, Y., Tamura, H., et al. 2004, *AJ*, 128, 2073, doi: [10.1086/424935](https://doi.org/10.1086/424935)
- Hayes, M., Schaerer, D., Östlin, G., et al. 2011, *ApJ*, 730, 8, doi: [10.1088/0004-637X/730/1/8](https://doi.org/10.1088/0004-637X/730/1/8)
- Hayes, M., Östlin, G., Schaerer, D., et al. 2013, *ApJL*, 765, L27, doi: [10.1088/2041-8205/765/2/L27](https://doi.org/10.1088/2041-8205/765/2/L27)
- Hayes, M., Östlin, G., Duval, F., et al. 2014, *ApJ*, 782, 6, doi: [10.1088/0004-637X/782/1/6](https://doi.org/10.1088/0004-637X/782/1/6)
- Higuchi, R., Ouchi, M., Ono, Y., et al. 2019, *ApJ*, 879, 28, doi: [10.3847/1538-4357/ab2192](https://doi.org/10.3847/1538-4357/ab2192)
- Inoue, A. K., Shimizu, I., Iwata, I., & Tanaka, M. 2014, *MNRAS*, 442, 1805, doi: [10.1093/mnras/stu936](https://doi.org/10.1093/mnras/stu936)
- Inoue, A. K., Hasegawa, K., Ishiyama, T., et al. 2018, *PASJ*, 70, 55, doi: [10.1093/pasj/psy048](https://doi.org/10.1093/pasj/psy048)
- Inoue, A. K., Yamanaka, S., Ouchi, M., et al. 2020, *PASJ*, 72, 101, doi: [10.1093/pasj/psaa100](https://doi.org/10.1093/pasj/psaa100)
- Itoh, R., Ouchi, M., Zhang, H., et al. 2018, *ApJ*, 867, 46, doi: [10.3847/1538-4357/aadfe4](https://doi.org/10.3847/1538-4357/aadfe4)
- Jeeson-Daniel, A., Ciardi, B., Maio, U., et al. 2012, *MNRAS*, 424, 2193, doi: [10.1111/j.1365-2966.2012.21378.x](https://doi.org/10.1111/j.1365-2966.2012.21378.x)
- Jiang, L., Egami, E., Fan, X., et al. 2013, *ApJ*, 773, 153, doi: [10.1088/0004-637X/773/2/153](https://doi.org/10.1088/0004-637X/773/2/153)
- Kakiichi, K., & Dijkstra, M. 2018, *MNRAS*, 480, 5140, doi: [10.1093/mnras/sty2214](https://doi.org/10.1093/mnras/sty2214)
- Kakuma, R., Ouchi, M., Harikane, Y., et al. 2021, arXiv e-prints, arXiv:1906.00173, <https://arxiv.org/abs/1906.00173>
- Kikuta, S., Matsuda, Y., Cen, R., et al. 2019, *PASJ*, 71, L2, doi: [10.1093/pasj/psz055](https://doi.org/10.1093/pasj/psz055)
- Kollmeier, J. A., Zheng, Z., Davé, R., et al. 2010, *ApJ*, 708, 1048, doi: [10.1088/0004-637X/708/2/1048](https://doi.org/10.1088/0004-637X/708/2/1048)
- Konno, A., Ouchi, M., Nakajima, K., et al. 2016, *ApJ*, 823, 20, doi: [10.3847/0004-637X/823/1/20](https://doi.org/10.3847/0004-637X/823/1/20)
- Konno, A., Ouchi, M., Shibuya, T., et al. 2018, *PASJ*, 70, S16, doi: [10.1093/pasj/psx131](https://doi.org/10.1093/pasj/psx131)

- Kovetz, E. D., Viero, M. P., Lidz, A., et al. 2017, arXiv e-prints, arXiv:1709.09066.
<https://arxiv.org/abs/1709.09066>
- Kusakabe, H., Shimasaku, K., Ouchi, M., et al. 2018, PASJ, 70, 4, doi: [10.1093/pasj/psx148](https://doi.org/10.1093/pasj/psx148)
- Kusakabe, H., Shimasaku, K., Momose, R., et al. 2019, PASJ, 71, 55, doi: [10.1093/pasj/psz029](https://doi.org/10.1093/pasj/psz029)
- Lake, E., Zheng, Z., Cen, R., et al. 2015, ApJ, 806, 46, doi: [10.1088/0004-637X/806/1/46](https://doi.org/10.1088/0004-637X/806/1/46)
- Laursen, P., & Sommer-Larsen, J. 2007, ApJL, 657, L69, doi: [10.1086/513191](https://doi.org/10.1086/513191)
- Laursen, P., Sommer-Larsen, J., & Razoumov, A. O. 2011, ApJ, 728, 52, doi: [10.1088/0004-637X/728/1/52](https://doi.org/10.1088/0004-637X/728/1/52)
- Leclercq, F., Bacon, R., Wisotzki, L., et al. 2017, A&A, 608, A8, doi: [10.1051/0004-6361/201731480](https://doi.org/10.1051/0004-6361/201731480)
- Leclercq, F., Bacon, R., Verhamme, A., et al. 2020, A&A, 635, A82, doi: [10.1051/0004-6361/201937339](https://doi.org/10.1051/0004-6361/201937339)
- Li, T. Y., Wechsler, R. H., Devaraj, K., & Church, S. E. 2016, ApJ, 817, 169, doi: [10.3847/0004-637X/817/2/169](https://doi.org/10.3847/0004-637X/817/2/169)
- Martin, D. C., Chang, D., Matuszewski, M., et al. 2014, ApJ, 786, 107, doi: [10.1088/0004-637X/786/2/107](https://doi.org/10.1088/0004-637X/786/2/107)
- Mas-Ribas, L., & Dijkstra, M. 2016, ApJ, 822, 84, doi: [10.3847/0004-637X/822/2/84](https://doi.org/10.3847/0004-637X/822/2/84)
- Mas-Ribas, L., Dijkstra, M., Hennawi, J. F., et al. 2017a, ApJ, 841, 19, doi: [10.3847/1538-4357/aa704e](https://doi.org/10.3847/1538-4357/aa704e)
- Mas-Ribas, L., Hennawi, J. F., Dijkstra, M., et al. 2017b, ApJ, 846, 11, doi: [10.3847/1538-4357/aa8328](https://doi.org/10.3847/1538-4357/aa8328)
- Matsuda, Y., Yamada, T., Hayashino, T., et al. 2012, MNRAS, 425, 878, doi: [10.1111/j.1365-2966.2012.21143.x](https://doi.org/10.1111/j.1365-2966.2012.21143.x)
- Mitchell, P. D., Blaizot, J., Cadiou, C., et al. 2021, MNRAS, 501, 5757, doi: [10.1093/mnras/stab035](https://doi.org/10.1093/mnras/stab035)
- Momose, R., Shimasaku, K., Nagamine, K., et al. 2021a, ApJL, 912, L24, doi: [10.3847/2041-8213/abf04c](https://doi.org/10.3847/2041-8213/abf04c)
- Momose, R., Shimizu, I., Nagamine, K., et al. 2021b, ApJ, 911, 98, doi: [10.3847/1538-4357/abe1b9](https://doi.org/10.3847/1538-4357/abe1b9)
- Momose, R., Ouchi, M., Nakajima, K., et al. 2014, MNRAS, 442, 110, doi: [10.1093/mnras/stu825](https://doi.org/10.1093/mnras/stu825)
- . 2016, MNRAS, 457, 2318, doi: [10.1093/mnras/stw021](https://doi.org/10.1093/mnras/stw021)
- Navarro, J. F., Frenk, C. S., & White, S. D. M. 1997, ApJ, 490, 493, doi: [10.1086/304888](https://doi.org/10.1086/304888)
- Oke, J. B., & Gunn, J. E. 1983, ApJ, 266, 713, doi: [10.1086/160817](https://doi.org/10.1086/160817)
- Ono, Y., Itoh, R., Shibuya, T., et al. 2021, ApJ, 911, 78, doi: [10.3847/1538-4357/abea15](https://doi.org/10.3847/1538-4357/abea15)
- Östlin, G., Hayes, M., Kunth, D., et al. 2009, AJ, 138, 923, doi: [10.1088/0004-6256/138/3/923](https://doi.org/10.1088/0004-6256/138/3/923)
- Ouchi, M., Ono, Y., & Shibuya, T. 2020, ARA&A, 58, 617, doi: [10.1146/annurev-astro-032620-021859](https://doi.org/10.1146/annurev-astro-032620-021859)
- Ouchi, M., Shimasaku, K., Furusawa, H., et al. 2010, ApJ, 723, 869, doi: [10.1088/0004-637X/723/1/869](https://doi.org/10.1088/0004-637X/723/1/869)
- Ouchi, M., Harikane, Y., Shibuya, T., et al. 2018, PASJ, 70, S13, doi: [10.1093/pasj/psx074](https://doi.org/10.1093/pasj/psx074)
- Patrício, V., Richard, J., Verhamme, A., et al. 2016, MNRAS, 456, 4191, doi: [10.1093/mnras/stv2859](https://doi.org/10.1093/mnras/stv2859)
- Péroux, C., & Howk, J. C. 2020, ARA&A, 58, 363, doi: [10.1146/annurev-astro-021820-120014](https://doi.org/10.1146/annurev-astro-021820-120014)
- Pullen, A. R., Doré, O., & Bock, J. 2014, ApJ, 786, 111, doi: [10.1088/0004-637X/786/2/111](https://doi.org/10.1088/0004-637X/786/2/111)
- Rauch, M., Haehnelt, M., Bunker, A., et al. 2008, ApJ, 681, 856, doi: [10.1086/525846](https://doi.org/10.1086/525846)
- Rosdahl, J., & Blaizot, J. 2012, MNRAS, 423, 344, doi: [10.1111/j.1365-2966.2012.20883.x](https://doi.org/10.1111/j.1365-2966.2012.20883.x)
- Scoville, N., Aussel, H., Brusa, M., et al. 2007, ApJS, 172, 1, doi: [10.1086/516585](https://doi.org/10.1086/516585)
- Sekiguchi, K., Akiyama, M., Furusawa, H., et al. 2005, in Multiwavelength Mapping of Galaxy Formation and Evolution, ed. A. Renzini & R. Bender, 82, doi: [10.1007/10995020_12](https://doi.org/10.1007/10995020_12)
- Shibuya, T., Ouchi, M., Konno, A., et al. 2018a, PASJ, 70, S14, doi: [10.1093/pasj/psx122](https://doi.org/10.1093/pasj/psx122)
- Shibuya, T., Ouchi, M., Harikane, Y., et al. 2018b, PASJ, 70, S15, doi: [10.1093/pasj/psx107](https://doi.org/10.1093/pasj/psx107)
- Silva, M. B., Santos, M. G., Gong, Y., Cooray, A., & Bock, J. 2013, ApJ, 763, 132, doi: [10.1088/0004-637X/763/2/132](https://doi.org/10.1088/0004-637X/763/2/132)
- Smit, R., Swinbank, A. M., Massey, R., et al. 2017, MNRAS, 467, 3306, doi: [10.1093/mnras/stx245](https://doi.org/10.1093/mnras/stx245)
- Smith, A., Ma, X., Bromm, V., et al. 2019, MNRAS, 484, 39, doi: [10.1093/mnras/sty3483](https://doi.org/10.1093/mnras/sty3483)
- Smith, A., Tsang, B. T. H., Bromm, V., & Milosavljević, M. 2018, MNRAS, 479, 2065, doi: [10.1093/mnras/sty1509](https://doi.org/10.1093/mnras/sty1509)
- Steidel, C. C., Bogosavljević, M., Shapley, A. E., et al. 2011, ApJ, 736, 160, doi: [10.1088/0004-637X/736/2/160](https://doi.org/10.1088/0004-637X/736/2/160)
- Steidel, C. C., Erb, D. K., Shapley, A. E., et al. 2010, ApJ, 717, 289, doi: [10.1088/0004-637X/717/1/289](https://doi.org/10.1088/0004-637X/717/1/289)
- Swinbank, A. M., Bower, R. G., Smith, G. P., et al. 2007, MNRAS, 376, 479, doi: [10.1111/j.1365-2966.2007.11454.x](https://doi.org/10.1111/j.1365-2966.2007.11454.x)
- Tumlinson, J., Peebles, M. S., & Werk, J. K. 2017, ARA&A, 55, 389, doi: [10.1146/annurev-astro-091916-055240](https://doi.org/10.1146/annurev-astro-091916-055240)
- Verhamme, A., Dubois, Y., Blaizot, J., et al. 2012, A&A, 546, A111, doi: [10.1051/0004-6361/201218783](https://doi.org/10.1051/0004-6361/201218783)
- Wisotzki, L., Bacon, R., Blaizot, J., et al. 2016, A&A, 587, A98, doi: [10.1051/0004-6361/201527384](https://doi.org/10.1051/0004-6361/201527384)
- Wisotzki, L., Bacon, R., Brinchmann, J., et al. 2018, Nature, 562, 229, doi: [10.1038/s41586-018-0564-6](https://doi.org/10.1038/s41586-018-0564-6)
- Wu, J., Jiang, L., & Ning, Y. 2020, ApJ, 891, 105, doi: [10.3847/1538-4357/ab7333](https://doi.org/10.3847/1538-4357/ab7333)
- Xue, R., Lee, K.-S., Dey, A., et al. 2017, ApJ, 837, 172, doi: [10.3847/1538-4357/837/2/172](https://doi.org/10.3847/1538-4357/837/2/172)

Zhang, H., Ouchi, M., Itoh, R., et al. 2020, ApJ, 891, 177,
doi: [10.3847/1538-4357/ab7917](https://doi.org/10.3847/1538-4357/ab7917)

Zheng, Z., Cen, R., Weinberg, D., Trac, H., &
Miralda-Escudé, J. 2011, ApJ, 739, 62,
doi: [10.1088/0004-637X/739/2/62](https://doi.org/10.1088/0004-637X/739/2/62)